Published in final edited form as:

Nature. 2014 May 1; 509(7498): 43–48. doi:10.1038/nature13276.

Presynaptic inhibition of spinal sensory feedback ensures smooth movement

Andrew J. P. Fink[1], **Katherine R. Croce**[1], **Z. Josh Huang**[2], **L. F. Abbott**[3], **Thomas M. Jessell**[1], and **Eiman Azim**[1]

[1]Howard Hughes Medical Institute, Kavli Institute for Brain Science, Mortimer B. Zuckerman Mind, Brain Behavior Institute, Departments of Neuroscience and Biochemistry and Molecular Biophysics, Columbia University, New York, New York 10032

[2]Cold Spring Harbor Laboratory, Cold Spring Harbor, New York 11724

[3]Center for Theoretical Neuroscience, Departments of Physiology and Neuroscience, Columbia University, New York, New York 10032

Abstract

The precision of skilled movement depends on sensory feedback and its refinement by local inhibitory microcircuits. One specialized set of spinal GABAergic interneurons forms axo-axonic contacts with the central terminals of sensory afferents, exerting presynaptic inhibitory control over sensory-motor transmission. The inability to achieve selective access to the GABAergic neurons responsible for this unorthodox inhibitory mechanism has left unresolved the contribution of presynaptic inhibition to motor behavior. We used *Gad2* as a genetic entry point to manipulate the interneurons that contact sensory terminals, and show that activation of these interneurons in mice elicits the defining physiological characteristics of presynaptic inhibition. Selective genetic ablation of *Gad2*-expressing interneurons severely perturbs goal-directed reaching movements, uncovering a pronounced and stereotypic forelimb motor oscillation, the core features of which are captured by modeling the consequences of sensory feedback at high gain. Our findings define the neural substrate of a genetically hard-wired gain control system crucial for the smooth execution of movement.

Animals execute skilled limb movements with seemingly effortless precision, belying an elaborate series of neural transformations that direct each motor act. Spinal motor output relies on local inhibitory interneurons that shape the response of motor neurons to diverse excitatory inputs[1]. Most inhibitory interneurons form direct postsynaptic connections with motor or premotor neurons[2], but a small subset of GABAergic interneurons instead forms

Correspondence and requests for materials should be addressed to T.M.J. (tmj1@columbia.edu) or A.F. (af2243@columbia.edu).

Supplementary Information is available in the online version of the paper.

Author Contributions A.F. and T.M.J. devised the project. A.F., E.A. and T.M.J. designed the experiments and analyzed the data. A.F. performed the anatomical and electrophysiological experiments. E.A. developed the behavioral assay and with A.F. and K.R.C. performed the behavioral experiments. L.F.A. developed and with A.F. implemented the computational models. Z.J.H. generated the $Gad2^{Cre}$ mouse. A.F., E.A., L.F.A and T.M.J. prepared the manuscript.

axo-axonic contacts with sensory afferent terminals, regulating sensory-motor drive through a process of presynaptic inhibition (Fig. 1a)[3,4]. This presynaptic inhibitory system can be recruited by sensory, descending and local neuronal inputs[4–6], implying its pivotal role in the control of motor output. But despite the occurrence of axo-axonic contacts at most sensory terminals[7,8], the predominance of postsynaptic inhibition has left unresolved the motor behavioral significance of this presynaptic control system.

Presynaptic inhibition has been characterized most extensively at proprioceptive sensory-motor synapses[3,4,6]. Proprioceptors convey the state of muscle contraction to motor neurons, through direct and indirect feedback pathways[1,9]. Elimination of proprioceptive feedback impairs motor coordination[10], establishing a basal requirement for sensory transmission in motor control. Conversely, limiting the gain of proprioceptive feedback has been proposed, on theoretical grounds, to be a critical determinant of motor stability[11]. In principle, the divisive nature of presynaptic inhibition provides an effective means of controlling sensory gain[9,12–14], but without a way to manipulate the relevant set of inhibitory interneurons it has not been possible to resolve whether, or how, presynaptic inhibition contributes to motor behavior.

The inhibitory interneurons that form axo-axonic contacts with sensory terminals differ from other spinal GABAergic neurons in that they alone express GAD2 (GAD65), one of two GABA-synthetic enzymes (Fig. 1a–c)[7,15,16]. We have used *Gad2* as a genetic entry point for manipulating presynaptic inhibitory interneurons in mice and assessing their role in motor behavior. Our findings indicate that *Gad2*-expressing interneurons mediate presynaptic inhibition at sensory-motor synapses, and that selective elimination of these interneurons elicits motor oscillations during goal-directed reaching. The essential features of this motor perturbation can be captured by a simple model in which high gain proprioceptive feedback induces limb oscillation. This alignment of behavior and theory argues that presynaptic inhibitory interneurons ensure the smooth operation of goal-directed motor behaviors by modulating the gain of sensory feedback.

Targeting GABApre neurons

We first asked whether the GABAergic interneurons that contact sensory terminals (GABApre neurons) can be defined by transgene reporter expression in a *Gad2-IRES-Cre* (*Gad2*^{Cre}) mouse line[17]. To mark *Gad2*-expressing interneurons (*Gad2*^{Cre} neurons) we injected a recombinant adeno-associated viral (AAV) vector encoding a Cre-recombinase-dependent (*FLEX*) channelrhodopsin (ChR2)-YFP fusion protein into the spinal cord of *Gad2*^{Cre} mice.

For physiological studies of presynaptic inhibition we targeted *Gad2*^{Cre} neurons in early postnatal lumbar spinal cord (Supplementary Note 1)[18]. At this stage *Gad2* is expressed both by GABApre neurons as well as by GABApost neurons that contact motor neurons and premotor interneurons (Fig. 1a–c)[7,19]. Injection of *FLEX-ChR2-YFP* into p0–3 lumbar segments resulted, 14–21 days later, in broad YFP expression with dense axonal labeling in the vicinity of motor neurons (Fig. 1d). At this stage 36% of GABAergic terminals near motor neurons derive from GABApre, and 64% from GABApost, neurons. We found that

85% of GABApre and 57% of GABApost boutons in ventral spinal cord expressed ChR2-YFP (Fig. 1b–f). Thus early postnatal *FLEX-ChR2-YFP* injection marks GABApre and GABApost boutons at similar incidence.

For motor behavioral studies we targeted *Gad2*^{Cre} neurons in adult cervical spinal cord (Supplementary Note 1 and Extended Data Fig. 1). Cervical injection of *FLEX-ChR2-YFP* at p56–84, with analysis 14–21 days later, revealed that 78% of GABApre and <1% of GABApost boutons expressed YFP (Fig. 1b,c,g–i). Thus adult *Gad2*^{Cre} transduction marks GABApre neurons in a near-selective manner.

Gad2^{Cre}-mediated presynaptic inhibition

We determined whether activation of *Gad2*^{Cre} interneurons elicits the two hallmarks of presynaptic inhibition: primary afferent depolarization and suppression of sensory neurotransmitter release[4].

We first examined whether photoactivation of ChR2-expressing *Gad2*^{Cre} neurons entrains neuronal spiking. Recordings from ChR2-YFP^{+} neurons in p9–14 lumbar spinal cord preparations from *Gad2*^{Cre} mice injected with *FLEX-ChR2-YFP* at p0–3 (Fig. 2a) revealed that photostimulation (473 nm, ~10 mW) elicited action potentials that followed frequencies up to ~50 Hz (Fig. 2b–d)[20]. Thus targeted ChR2 expression confers optical control of *Gad2*^{Cre} neuronal spiking.

We then determined whether GABA released upon *Gad2*^{Cre} neuronal photoactivation depolarizes sensory neurons, eliciting primary afferent depolarization (PAD; Fig. 2e)[21]. Single pulse photoactivation of *Gad2*^{Cre} interneurons elicited PAD with an amplitude and time course similar to that induced by dorsal root simulation (Fig 2e,f). Antagonists of GABA-A receptors, but not glycine receptors, abolished *Gad2*^{Cre} neuron-evoked PAD (Fig. 2g), establishing its GABAergic character[22]. But PAD reflects the depolarization of cutaneous as well as proprioceptive afferents[21], prompting us to ask whether *Gad2*^{Cre} neuron activation depolarizes proprioceptive afferents. At reduced temperatures *in vivo* PAD evokes transmitter release from proprioceptor terminals, depolarizing motor neurons (Supplementary Note 2)[21]. Consistent with this, we found that *Gad2*^{Cre} photoactivation *in vitro* at 24–26°C elicited a GABA-A and AMPA receptor-dependent motor neuron depolarization (Extended Data Fig. 2). Thus activation of *Gad2*^{Cre} neurons elicits PAD at proprioceptor terminals.

To assess the impact of *Gad2*^{Cre} neuronal activation on sensory-motor transmission we isolated sensory input to motor neurons. Stimulation of individual L3 to L5 dorsal roots elicited monosynaptic excitatory postsynaptic currents (EPSCs) in motor neurons (mean amplitude 1.2 ± 0.3 nA s.e.m.; cv_{onset} < 0.02; n = 19; Fig. 2h–k and Extended Data Fig. 3)[23]. Photoactivation of *Gad2*^{Cre} neurons elicited a frequency-dependent reduction in sensory-evoked EPSC amplitude that persisted for >800 ms (Fig. 2l, inset: mean ~40%, range 19%–53% reduction in EPSC amplitude; two-tailed paired t test, $P < 10^{-4}$, n = 9; Extended Data Fig. 4). Thus synchronous activation of *Gad2*^{Cre} neurons elicits a long-lasting suppression of sensory-evoked EPSCs (Supplementary Note 3).

At the neonatal stages used for physiological analysis *Gad2*^{Cre} marks both GABApre and GABApost neurons. Nevertheless, three findings indicate that *Gad2*^{Cre} suppression of sensory-evoked EPSCs reflects presynaptic inhibition. First, *Gad2*^{Cre}-evoked inhibitory postsynaptic currents (*Gad2*^{Cre}-IPSCs) persisted for only ~30 ms (Fig. 3a–c and Extended Data Fig. 5a–c), whereas *Gad2*^{Cre} EPSC suppression lasted long after *Gad2*^{Cre}-IPSCs have decayed (Extended Data Fig. 4a, 5a,b)[4]. Second, *Gad2*^{Cre} EPSC suppression is exclusively GABAergic, whereas coexpression of glycine by most GABApost neurons[24,25] underlies the fact that *Gad2*^{Cre}-IPSCs are predominantly glycinergic (Fig. 3a–g). Third, *Gad2*^{Cre} EPSC suppression did not alter EPSC waveforms, arguing against the idea that the reduction in EPSC amplitude reflects an increased motor neuron membrane conductance (Extended Data Fig. 5d–j). These findings reveal that GABApost neurons make only a minimal contribution to the inhibition of sensory-evoked EPSCs, thus implicating GABApre neurons.

The second core feature of presynaptic inhibition is a reduced probability of sensory transmitter release[26,27]. Modeling shows that this reduction can be captured by the kinetics of decay in amplitude of successive sensory-evoked EPSCs (Fig. 3h,i)[28,29]. We found that upon repetitive dorsal root stimulation, photoactivation of *Gad2*^{Cre} neurons elicited a reduction in the rate of EPSC amplitude decay that was readily fit by a decrease in the release probability parameter of a short-term depression model (p_r = 0.69 ± 0.03, control; 0.50 ± 0.05 s.e.m., photoactivation; two-tailed paired *t* test, $P < 0.001$, $n = 9$; Fig. 3i,j and Extended Data Fig. 6)[29]. The fidelity of this fit indicates that activation of *Gad2*^{Cre} neurons reduces sensory transmitter release probability. Thus *Gad2*^{Cre} neurons mediate both classical features of presynaptic inhibition at sensory-motor synapses.

Limb oscillation after GABApre ablation

In primates presynaptic inhibition has been implicated in the control of forelimb movement[30], prompting us to use goal-directed reaching in mice as a behavioral routine for examining the impact of removing presynaptic inhibition (Supplementary Note 1). We eliminated GABApre neurons by injecting an AAV encoding a Cre-recombinase-dependent diphtheria toxin receptor-GFP fusion (*FLEX-DTR-GFP*) unilaterally into C3–T1 spinal segments in p56–84 *Gad2*^{Cre} mice (Fig. 4a)[31]. Administration of diphtheria toxin (DT) 14–21 days later resulted in a >90% depletion of GAD2^{+}/GAD1^{+} boutons on ventral vGluT1^{+} sensory terminals, without altering the number of GABApost GAD2^{OFF}/GAD1^{+} boutons (Fig. 4b). Thus adult *Gad2*^{Cre}-based DTR targeting achieves selective elimination of GABApre neurons. Mice lacking GABApre neurons exhibited two prominent behavioral phenotypes: impaired reaching and forelimb scratching.

To analyze forelimb motor behavior, mice were trained to reach for and retrieve a food pellet located on the far side of a narrow access window[31,32], with reaches analyzed before and after GABApre neuronal ablation (Fig. 4c,d). DT administration elicited a dramatic degradation in reach accuracy, such that by the seventh post-DT day <5% of trials were successful, compared to a pre-DT success rate of ~50% (Fig. 4e). We detected no change in left-right forelimb alternation, nor in the accuracy of forepaw placement in a horizontal ladder stepping task (Fig. 4f)[31,33]. While these findings do not preclude a role for

presynaptic inhibition in locomotor control, they do indicate a degree of task-selectivity in the degradation of motor performance.

To evaluate forelimb movement we quantified limb kinematics by tracking a reflective marker attached to the right forepaw (Fig. 4d)[31], comparing reach trajectory and velocity in individual mice before and after GABApre ablation. Before DT administration mice displayed smooth paw trajectories that varied little across trials or with trial success (Extended Data Fig. 7a and Supplementary Videos 1,2)[31]. In contrast, after GABApre ablation the stereotypic smooth nature of reaches was lost and paw trajectories exhibited frequent reversals in direction (Fig. 5a–c, Extended Data Fig. 7b, Extended Data Table 1 and Supplementary Videos 3,4). Kinematic defects were restricted to the 'reach' phase – prior to the point that the paw passes through the access window (Fig. 5c and Extended Data Table 1). We observed no perturbation of the limb at rest; during the initiation of forelimb movement; during the late 'grab' phase – when the paw pronates in anticipation of pellet grasp; nor in digit abduction during grasp attempts (Fig. 5b–e, Extended Data Table 1 and Supplementary Video 5; see Methods and Supplementary Discussion).

To assess the periodicity of aberrant forelimb movements upon GABApre ablation we examined the temporal structure of forepaw kinematics. The spectral power of pre-DT reaches decayed steadily with increasing oscillation frequency (Fig. 5f,g). In contrast, post-DT reach oscillations exhibited an ~7.4-fold increase in peak spectral amplitude within the 18–22 Hz frequency range, focused at 19.5 ± 0.5 Hz s.e.m., with little variability across reaches and animals ($cv_{frequency}$ = 0.06, n = 5; Fig. 5f,g). We also detected a subharmonic series with spectral peaks at 10.8 ± 0.5 Hz and 5.9 ± 0.3 Hz (Fig. 5f). The decay of post-DT oscillations could be fit by a single exponential function with a time constant of 77 ± 3 ms s.e.m., again consistent across animals (cv_{decay} = 0.08, n = 5; Fig. 5h,i). Thus elimination of GABApre neurons uncovers a structured oscillation of constant frequency and decay time – defining features of a damped harmonic oscillator.

A GABApre gain control system

Prior models of sensory-motor control have proposed that increasing the gain of proprioceptive feedback elicits motor oscillation[11]. Can a simple model of sensory-motor feedback gain provide a theoretical framework for interpreting the oscillations that follow GABApre ablation? We simulated a simplified forelimb joint controlled by flexor and extensor torques and subject to gain-modulated sensory feedback, fitting the frequency and decay time of the model's single oscillatory eigenmode to experimentally-derived post-DT values (Fig. 6a,b, Extended Data Fig. 8a,b and Supplementary Note 4). At low feedback gain this model displayed smooth joint extension, resembling pre-DT reach velocity profiles (Fig. 6a,c; compare with Fig. 5d, top). At high gain, simulating the loss of divisive (presynaptic) inhibition, joint extension was dominated by a cycle of flexor-extensor alternation that resembled post-DT reach velocity profiles (Fig. 6b,d; compare with Fig. 5d, bottom, Supplementary Note 4). Reducing subtractive (postsynaptic) inhibition did not result in similar oscillations (Fig. 6c, green line, Supplementary Note 4 and Supplementary Discussion). This theoretical analysis suggests that oscillations produced by elimination of

presynaptic inhibition cannot be compensated by remaining intact postsynaptic inhibition, consistent with our experimental observations.

How do joint oscillations evolve as gain increases? Across a wide range of gain levels, the oscillatory frequency and decay times were constrained to a narrow set of values (Fig. 6e,f and Supplementary Note 4), providing a potential basis for the constancy of motor oscillation observed across mice. Moreover, similar oscillations emerged across multiple feedback delays (Extended Data Fig. 8c–h), accommodating the potential involvement of direct and indirect sensory feedback circuits (Supplementary Note 5). Thus a simple model of proprioceptive feedback-driven oscillation can account for the principal motor deficits that emerge upon elimination of presynaptic inhibition.

Finally, we considered whether this propriocentric view of feedback-driven oscillation is challenged by the forelimb scratching behavior observed after GABApre ablation (Extended Data Fig. 9a,b). In particular, we asked whether defects in forelimb reach could reflect enhanced cutaneous input. We applied the Na^+ channel blocker lidocaine topically to the forelimb of GABApre-ablated mice, with the intent of selectively inactivating cutaneous sensory endings. Lidocaine eliminated scratching behavior but left reaching defects and the ~20 Hz forelimb oscillation unaffected (Extended Data Fig. 9c–f and Supplementary Video 6). These results argue against the notion that enhanced cutaneous gain contributes to motor oscillation and aberrant reaching. Our findings therefore place GABApre neurons at the core of a proprioceptive gain control system for suppression of oscillations during goal-directed forelimb movement.

Discussion

Despite long appreciation of presynaptic inhibitory control, its contribution to motor behavior has remained unclear. We have identified, activated and eliminated the spinal GABAergic interneurons responsible for presynaptic inhibition at sensory synapses, revealing their central role in suppressing motor oscillation during forelimb movement. Our findings address three core issues in sensory-motor control: the behavioral relevance of sensory gain scaling; the neural underpinnings of smooth limb trajectory; and the grain of neural circuitry that engages presynaptic inhibition.

The rich repertoire of mammalian limb movements demands that proprioceptive afferents sustain a wide range of firing frequencies as they strive to supply task-appropriate feedback[34]. The dynamic character of sensory firing implies in principle that the strength of presynaptic inhibition should scale with the intensity of sensory input[35,36]. Several strategies underlie the dynamic scaling of sensory feedback gain by GABApre neurons. At a circuit level GABApre neurons can be driven to high firing rates by proprioceptive input[37], and our physiological studies reveal a strict proportionality between the frequency of GABApre neuronal spiking and the strength of presynaptic inhibition. These two features suggest that GABApre neurons scale sensory input gain in register with proprioceptor firing frequency. At a synaptic level, the prolonged time-course of presynaptic inhibition has the consequence that gain changes endure despite rapid fluctuation in sensory firing frequency over the course of a movement (Supplementary Note 3). The rapid spiking sustained by GABApre

neurons also provides insight into the selectivity of expression of GAD2: by virtue of its association with synaptic vesicles GAD2 facilitates GABA release at high firing frequencies[16,38]. Thus both the microcircuitry and neurochemistry of GABApre neurons contribute to the adaptive scaling of sensory feedback during motor control.

Motor circuits throughout the CNS are prone to oscillation[39–41]. Yet the smoothness that normally characterizes limb trajectories implies that oscillations are suppressed prior to motor neuron activation[42]. Behavioral studies, in conjunction with modeling, suggest that the GABApre gain control system provides one effective means of suppressing forelimb oscillation. We observe that mice at rest lack an overt tremor, consistent with the idea that oscillations are driven by proprioceptive feedback, a central tenet of the gain model. Moreover, the shallow relationship between gain and oscillation revealed by modeling offers a plausible explanation for the observed constancy of oscillation frequency and decay across GABApre-depleted mice. While the linear nature of the model explains primary oscillatory peak frequency, it leaves open the origins of sub-harmonic peaks. During periodic cycles of movement, sensory input occasionally fails to drive supra-threshold motor neuron activation[43], suggesting that sub-harmonics could have their basis in the intermittent skipping of one or more feedback-driven oscillatory cycles. Taken together, a simple model of sensory gain control provides theoretical support for the idea that GABApre neurons play a crucial role in ensuring smooth movement.

We note that the impact of manipulating presynaptic inhibition appears highly selective. Forelimb oscillations emerge after GABApre ablation despite the persistence of postsynaptic inhibition. Parallel theoretical and experimental analyses show that the subtractive nature of postsynaptic inhibition is far less effective in gain scaling than the divisive normalization achieved by presynaptic inhibition (Supplementary Discussion)[12–14]. Moreover, experimental inactivation of other defined spinal interneuron subtypes, both excitatory and inhibitory, impairs motor performance without obvious limb oscillation[31,44–46], implying a specialized contribution of presynaptic inhibition to smooth movement. Our findings also reveal the modular nature of skilled reach – in that oscillations after GABApre ablation are evident only during the forelimb reach phase, leaving the initiation and later grab phases unscathed. Such modular selectivity implies contextual recruitment of presynaptic inhibition during movement, permitting flexibility in the scaling of sensory gain (Supplementary Discussion)[13]. The precision of recruitment of GABApre neurons by sensory and descending pathways[4–6,47–50], when coupled with the diversity of sensory neurons influenced by presynaptic inhibition[6], hints at the existence of many GABApre neuronal subtypes, each devoted to gain control across discrete sensory feedback channels.

Methods

Mice

Gad2::IRES::Cre[17] (*Gad2*^{Cre}) and *Hb9::GFP*[51] (*Hb9*^{GFP}) mice were all on a C57BL/6 background. Animals were housed individually with light on a 12:12 hour cycle. For electrophysiology experiments, *Gad2*$^{Cre/Cre}$ homozygous mice were paired for breeding. Procedures performed in this study were conducted according to US National Institutes of

Health guidelines for animal research and were approved by the Institutional Animal Care and Use Committee of Columbia University.

Viral Vectors

To mark Cre-recombinase expressing neurons in *Gad2^{Cre}* mice for photoactivation or anatomical tracing, we used an AAV construct in which an inverted *hChR2(H134R)-EYFP* sequence was flanked by two pairs of heterotypic antiparallel *loxP* recombination sites (K. Deisseroth; Addgene plasmid 20298). *AAV-FLEX-hChR2-YFP* (*FLEX-ChR2-YFP*) was packaged and pseudotyped with an AAV1 serotype to a titer of 4×10^{12} viral particles/ml (UNC Gene Therapy Center). For anatomical analysis and photoactivation experiments we performed *FLEX-ChR2-YFP* injection at p0–p3 into lumbar spinal cord. For anatomical tracing of GABApre neurons we performed *FLEX-ChR2-YFP* injection at p21–p30 into lumbar spinal cord and p56–84 into cervical spinal cord.

To mark *Gad2^{Cre}* neurons for acute ablation we generated a Cre-dependent *AAV-FLEX-DTR-GFP* (*FLEX-DTR-GFP*), in which a simian *DTR (HBEGF)* sequence was fused to *GFP*. Details for the construction of the *FLEX-DTR-GFP* construct are described elsewhere[31]. Briefly, the insert was flanked by two pairs of heterotypic, antiparallel *loxP* recombination sites, downstream of a *CAG* promoter and upstream of a *woodchuck hepatitis virus post-transcriptional regulatory element (WPRE)* sequence. After confirming Cre-mediated expression specificity, the virus was packaged and pseudotyped with an AAV1 serotype to a titer of 5×10^{12} viral particles/ml (UNC Gene Therapy Center). To drive DTR expression in *Gad2^{Cre}* neurons we performed *FLEX-DTR-GFP* injection at p56–84 into cervical spinal cord.

Lumbar viral injections for photoactivation and anatomical experiments

Gad2^{Cre} pregnant females were housed individually ~5 days before giving birth and given additional bedding materials to encourage nest building.

Before removing pups from the nest, the mother was placed in a separate cage so as not to be disturbed. Pups were placed on a heating pad and anesthetized with isoflurane. For injections, the feet and head of the pup were taped to a paper towel placed on the heating pad to gently stretch the vertebral column. A small, longitudinal incision was made in the skin between the hips and shoulder, directly over the spinal cord. Connective tissue covering the vertebral column was gently removed using fine scissors and the skin flaps were retracted to expose the vertebrae. The last rib was identified and used to locate the L1 vertebral lamina.

Injections were performed using a Nanoject II (Drummond Scientific Company) placed in a stereotaxic arm (Narishege) with glass capillaries pulled using a P-30 vertical puller (Sutter) and then cut under a dissection stereomicroscope with fine scissors to ensure a sharp point. The Nanoject II was set to deliver 23 nl of solution per injection on the slow setting.

We targeted our injections to the medial portion of the spinal cord where GABApre neurons reside. We positioned the tip of the capillary 50 μm to the right of midline and in between the laminae (at this young age, it is possible to insert the fine capillary needle directly in

between the laminae into the spinal cord). We then penetrated 1200 μm into the tissue and injected 23 nl of solution every 100 μm while retracting. Following each injection we waited 10 seconds to allow diffusion of the solution. At the top of each injection track we waited for 1 minute to allow for diffusion of the solution and to prevent virus from exiting the cord with the capillary. Injections were performed at the three laminae above and below the L1 vertebra, permitting delivery of virus throughout the lumbar spinal cord. The incision was then closed using four inside-out sutures, and the pups were allowed to recover on the heating pad until awake, at which point they were returned to the nest. Only after several minutes of rehabituation to the nest was the mother reintroduced to the home cage.

To characterize the population of *Gad2*-expressing neurons at later ages, we injected *FLEX-ChR2-YFP* into lumbar spinal cord at p21–30. Mice were anesthetized with isoflurane and hair was removed. To prevent dryness of the eyes, eye lubricant (Puralube Vet Ointment; Dechra) was applied. Similar to neonate injections, the animal was securely positioned by gently taping the hindlimbs, forelimbs, shoulders and hips, and an incision was made in the skin to expose lumbar and caudal thoracic spinal segments. It was not necessary to remove any muscle above the spinal vertebrae, although connective tissue covering the segments was typically removed to allow penetration of the glass capillary. Since the spinal cord is larger at these older ages, injections were made 1500 μm below the surface, every 100 μm, following the same procedure as at p0–3. Three segments rostral and caudal to the L1 vertebra were injected, resulting in AAV delivery to the full extent of the lumbar spinal cord.

Cervical viral injections for anatomical tracing and ablation experiments

A detailed description of the cervical injection procedure can be found elsewhere[31]. Briefly, for cervical spinal cord AAV injections, mice were anesthetized with 0.01 ml g^{-1} body weight of 2.5% tribromoethanol (Sigma-Aldrich) via intraperitoneal injection and maintained as needed. Eye lubricant was applied and the mice were placed in a stereotaxic frame (David Kopf Instruments). The head of the mouse was tilted forward and the tail was gently elevated and pulled back using a spinal vertebrae clamp (David Kopf Instruments). After making an incision in the skin covering the cervical spinal cord, the cervical laminae were exposed using forceps and a delicate bone scraper (Fine Science Tools). The laminae were cleaned with absorption spears (Fine Science Tools) and gently separated via retraction of the large spiny process of the second thoracic vertebra using a small alligator clip held in place by a spinal vertebrae clamp. After removal of the cervical dura mater using fine forceps, *FLEX-ChR2-YFP* virus (for anatomical tracing) or *FLEX-DTR-GFP* virus (for ablation experiments) was delivered to cervical spinal cord using a Nanoject II. Injections were restricted to the right side of the C3–T1 segments, with three injection traces per segment, 23 nl per injection, spanning the dorso-ventral extent of the cord.

For ablation experiments, approximately 14–21 days following *FLEX-DTR-GFP* injection, mice were administered 400 ng of diphtheria toxin (Sigma-Aldrich) in sterile phosphate buffered saline via intraperitoneal injection. For analysis of ablation efficiency, mice were perfused one week after DT administration and tissue was processed for immunohistochemistry.

Electrophysiology, dissection

To obtain whole-cell patch-clamp recordings from motor neurons with intact sensory input and interneuron circuitry, we developed an *in vitro* semi-intact spinal cord preparation that permitted recordings from spinal motor neurons under visual guidance. Mice aged p9–p14 were anesthetized with tribromoethanol (2.5% solution, 30 μl per gram body weight) and transcardially perfused using ice cold dissection artificial cerebral spinal fluid (dACSF) containing 234 mM sucrose, 3.6 mM KCl, 1.2 mM $NaH_2PO_4.H_2O$, 25 mM $NaHCO_3$, 11 mM D-Glucose, 0.5 mM $CaCl_2$, 4 mM $MgCl_2$, 0.4 mM ascorbic acid, 2 mM pyruvate, 20 μM APV and 5 mM kynurenic acid, and equilibrated with 95% O_2 and 5% CO_2. We found that effective transcardial perfusion was critical to obtain healthy motor neurons at these ages.

The vertebral column was then extracted and placed in a dissection dish superfused with oxygenated dACSF and cooled to ~2° Celsius using a custom made, chilled brass chamber (G. Johnson, Columbia University). The spinal cord and rib cage was pinned ventral side up in a Sylgard 184 Silicone Elastomer (Dow Corning) coated dissection dish and the corpora were removed. The thoracic and sacral portions of the spinal cord were removed and a longitudinal incision was made in the dura mater along the ventral surface of the lumbar spinal cord using fine Vannas scissors (FST). Using #55 forceps (FST) the dura was then peeled off of the ventral surface on the right side of the spinal cord, taking care not to damage the dorsal roots. The cord was then hemisected by passing a beveled crescent scalpel (Sharptome) through the midline. The dorsal roots on the right side were then cut and the right half of the cord gently removed from the vertebral column. The left hemicord was used in some experiments for ventral and dorsal root recordings, coupled with photoillumination of the exposed midline, following standard methods[18,52].

To expose motor neurons for whole-cell recordings we removed the ventral-lateral white matter. To prepare the tissue for cutting, we embedded the cord in 1.5% low melting point agarose made fresh in dACSF. We placed the hemicord in a 15 × 15 × 5 mm disposable base mold (Fisher) and carefully positioned it so that the ventral surface was facing down, towards the base of the mold. We then quickly replaced the dACSF with 1.5% LMP agar, siphoning off the dACSF with a Pasteur pipette and applying the warm, LMP agar with a plastic transfer pipette. Once the cord was in the LMP agar, but before the agar had hardened, we carefully lifted the dorsal roots away from the cutting plane, making sure that the cord was positioned so that the dorso-ventral axis was perpendicular to the bottom of the mold. We then placed the mold on a cold plate and covered the surface with a chilled glass coverslip to speed setting of the agar. It is important to place the mold on the cold plate once the cord and roots are in position, as the agar sets quickly. The mold and coverslip were then immediately submerged in ice cold, oxygenated dACSF and the coverslip was removed once the agar was sufficiently hardened (after about ten seconds). Submerged in the solution, the agar block containing the hemicord was then extracted from the mold using a small metal spatula.

The agar block was glued using Loctite 404 cyanoacrylate glue to an angled block cut from 4% agar (~25° angle) which itself had been glued to the chilled vibratome stage. The stage

was then quickly placed in ice cold, oxygenated dACSF in the vibratome bath. A vibratome (Leica VT1200) was used to remove the ventral-lateral white matter; the vibratome blade was positioned at the surface of the spinal cord, then lowered 50 μm below the surface and used to cut a sliver of white matter off of the hemicord. Cuts were made, typically between one and three, until a fine strip of grey matter was visible through a stereo dissection scope. The cut hemicord cord was then carefully removed from the 1.5% agarose and placed in recovery solution. The hemicord was then allowed to recover for 30 minutes at 34°C before being placed in the recording chamber (Warner) where it was superfused with recording ACSF containing 125 mM NaCl, 26 mM $NaHCO_3$, 1.25 mM NaH_2PO_4, 2.5 mM KCl, 2 mM $CaCl_2$, 1 mM $MgCl_2$, 0.4 mM ascorbic acid, 2 mM pyruvate and 26 mM D-glucose, and equilibrated with 95% O_2 and 5% CO_2. The recovery solution was a 50:50 mixture of ACSF and dASCF.

Electrophysiological recordings

The cord was placed in a laminar flow chamber (Warner) with the exposed ventral surface facing up and secured with a harp strung with fine, loose, nylon fibers. Dorsal roots L3, L4 and L5 were positioned within polyethylene suction electrodes for nerve stimulation. The suction electrodes were held using a custom made holder and miniature manipulators (G.Z. Mentis, Columbia University). A stimulus isolator (AMPI) was used to stimulate dorsal roots with 100 μs current pulses. Dorsal roots were stimulated at 1.2-fold threshold, with threshold defined as the stimulation intensity that generated a postsynaptic response in roughly 60% of trials[52]. Typically stimulation intensities were between 2 and 10 μAmps, depending on the size of the root and the seal of the suction electrode.

Whole-cell recordings were obtained using 2.5–3.5 MOhm pipettes pulled using a P-2000 puller (Sutter). An Olympus BX-51 microscope with an infrared DIC filter set was used to visualize motor neurons. A Multiclamp 700B amplifier and Digidata 1440A (Molecular Devices) were used to record and transfer electrical potentials to a desktop computer (Dell). Data were digitized at 20–50 kHz and a 10 kHz low-pass filter was used before digitization. Motor neurons were identified based on their ventral-lateral position, their large size and distinct dendritic morphology, their electrophysiological properties and their expression of GFP using $Hb9^{GFP}$ transgenic mice. Motor neurons typically had a resting membrane potential between −68 mV and −74 mV. Cells with a resting membrane potential more depolarized than −60 mV were discarded.

Voltage clamp experiments were performed using a cesium-methanesulfonate-based internal solution containing 135 mM $CesMeSO_3$, 5 mM $CsCl_2$, 2 mM NaCl, 10 mM HEPES, 0.1 mM EGTA, 4 mM MgATP, 0.4 mM Na_2GTP, 10 mM phosphocreatine and 5 mM QX-314 chloride. Motor neurons were held between −60 and −70 mV and recordings in which the series resistance exceeded 20 MOhm or increased by greater than 20% during a recording were excluded. Because of the large size and low input resistance of the motor neurons, as well as the magnitude of the synaptic currents, series resistance was monitored but not compensated. Current clamp recordings were performed using a potassium-gluconate-based internal solution with 130 mM potassium gluconate, 5 mM NaCl, 1 mM $CaCl_2$, 1 mM $MgCl_2$, 10 mM HEPES and 4 mM Na_2ATP. All experiments in which sensory-evoked

synaptic currents were isolated were performed using 20 μM APV (Tocris). Internal solutions were titrated to a pH of 7.4 with potassium hydroxide for the potassium-gluconate-based internal solution and cesium hydroxide for the cesium-methanesulfonate-based internal solution. Osmolarity was between 290 and 300 mOsm and was measured using a vapor pressure osmometer (Vapro).

To avoid potential confounds of voltage-gated channel activation during synaptic excitation, we applied internal blockage of voltage-gated potassium channels (via cesium) and sodium channels (via QX-314). However, blocking sodium and potassium channels increases motor neuron input resistance that, together with the high capacitance of spinal motor neurons due to their extreme size, results in prolonged membrane time constants. Under these conditions EPSPs, but not EPSCs, have an extended decay time. Thus, except for our mean variance analysis experiments (see below), we used voltage clamp to isolate monosynaptic sensory input to motor neurons.

Extracellular recordings from dorsal roots and ventral roots were obtained using the same suction electrodes used for nerve stimulation. Signals were amplified using a Cyberamp 320 extracellular amplifier (Molecular Devices) and were low-pass filtered at 10,000 kHz and in some cases high-pass filtered.

Drugs used: the GABA-A antagonist SR 95531 hydrobromide (gabazine, 2 μM), the GABA-B antagonist CGP 54626 (CGP, 2.5 μM), the glycine receptor antagonist strychnine (5 μM), the NMDA receptor antagonist APV (20 μM) and the AMPA receptor antagonist NBQX (10 μM) –all from Tocris.

Photostimulation was performed using a 473 nm diode laser (CrystaLaser) controlled by 5 Volt TTL pulses of varying duration. Laser strength was set to be suprathreshold for generation of IPSCs in motor neurons and pulse length was typically 1 ms, though in some experiments 5 ms pulses were used. For calibration of spiking responses of $Gad2^{Cre}$ neurons the laser pulse width was 1 ms. Recordings from $ChR2^{+}$ $Gad2^{Cre}$ neurons were obtained using a sagittal hemisected preparation[53] that permits targeted recordings from neurons residing near the midline. The central canal was identified and ChR2-YFP^{+} neurons residing within 200 μm dorsal and 100 μm lateral of the central canal were targeted. In some preparations we noted that IPSCs followed light pulse frequencies greater than 50 Hz, presumably due to high levels of ChR2 expression. We therefore used 100 Hz light pulses in some experiments to ensure maximal $Gad2^{Cre}$ neuron activation.

All electrophysiology data were analyzed in MATLAB (Mathworks). Sensory-evoked EPSC onset was calculated by identifying the time point at which the derivative of the EPSC waveform crossed a noise threshold (twice the variance of the derivative waveform in the 50 ms preceding stimulation) for five consecutive time bins. Monosynaptic inputs were identified based on the low variance of their trial-to-trial onset latency ($cv_{onset} < 0.05$)[23]. Coefficient of variation (*cv*) was calculated as the standard deviation divided by the mean throughout. The onset of IPSCs, as well as ventral root and dorsal root spikes, were estimated using a similar thresholding method. Instead of using the derivative trace, however, which was at times too noisy, onset was defined as the point where the current or

voltage waveform crossed a hand-picked threshold for five consecutive points. The estimated onset times were then checked by eye for each trace.

The IPSC index ($IPSC_{index}$, Fig. 3d) was calculated as follows, where $IPSC_{\lambda,\Phi}$ is the mean amplitude of light-evoked IPSCs in the presence of drug (either strychnine or SR 95531 and CGP 54626) and $IPSC_{\lambda}$ is the mean amplitude of light-evoked IPSCs in the absence of drug:

$$IPSC_{index}=\frac{IPSC_{\lambda,\Phi}}{IPSC_{\lambda}} \quad (1)$$

The EPSC index ($EPSC_{index}$, Fig. 3g) was calculated as follows, where $EPSC_{\lambda,\Phi}$ is the mean sensory-evoked EPSC amplitude following $Gad2^{Cre}$-neuron photoactivation and in the presence of drug, $EPSC_{\Phi}$ is the mean sensory-evoked EPSC amplitude without $Gad2^{Cre}$ neuron photoactivation in the presence of drug, $EPSC_{\lambda}$ is the mean sensory-evoked EPSC amplitude following $Gad2^{Cre}$ neuron photoactivation without drug and $EPSC$ is the mean sensory-evoked EPSC amplitude with neither $Gad2^{Cre}$ neuron photoactivation nor drug present:

$$EPSC_{index}=\frac{1-\frac{EPSC_{\lambda,\Phi}}{EPSC_{\Phi}}}{1-\frac{EPSC_{\lambda}}{EPSC}} \quad (2)$$

The value of the IPSC index is 1 when drug has no effect and 0 when the drug completely blocks the IPSC. The value of the EPSC index is 1 when drug has no effect on $Gad2^{Cre}$ neuron-mediated suppression of sensory-evoked EPSCs and 0 when drug application abolishes the suppression of sensory-evoked EPSCs achieved by $Gad2^{Cre}$ neuron photoactivation.

For intracellular recording data *n* values indicate neurons recorded. For extracellular root recordings *n* values indicate preparations.

Vesicle depletion model

The vesicle depletion model was adapted from previously described simulations[29,54] and was implemented in MATLAB. The model has three parameters: the time constant of facilitation, the time constant of depression and release probability. The facilitation time constant was not found to influence vesicle depletion at frequencies <25 Hz, and so was set to 10 ms. The depression time constant was set so that normalized synaptic conductances generated by the model matched by eye those from control (no photostimulation) electrophysiological data. We found that depression time constants between 125 ms and 975 ms with a mean of 437 ± 305 ms s.d. captured the depression kinetics we observed. To determine the release probability time constant, the average amplitudes of consecutive experimentally derived EPSCs were estimated. EPSC amplitudes were then generated using the vesicle depletion model and were fit with single exponential functions, which were then superimposed upon normalized EPSC amplitudes obtained from actual recordings. Changing the release probability parameter of the model, and the release probability parameter alone, was sufficient to capture light-evoked changes in the rate of synaptic depression.

Mean variance analysis

The mean variance analysis used was described previously[55]. Data was collected in current clamp to avoid measurement errors introduced by changes in series resistance over long recording sessions (Extended Data Fig. 6). Each calcium concentration was visited twice for a given cell, and EPSP amplitudes used for analysis were taken from two sets of 25 consecutive dorsal root stimuli once the amplitude had stabilized following introduction of a new calcium concentration. Quadratic functions were fit using standard curve fitting routines in MATLAB. The cv_q parameter in the mean variance analysis was set to 0.3, following established values[55]. Changes (± 10%) to this parameter did not dramatically affect the release probability estimates.

Kinematic analysis of reaching

The basic training paradigm and reaching box design were largely based on established methods[32,33], and were adapted to 3D kinematic analyses in the mouse, as described[31].

Briefly, adult mice (~12–20 weeks old) were food deprived to ~80–90% of their original body weight and habituated to target food pellets (20 mg, 3 mm diameter; Bio-Serv). Approximately 3g of pellets were provided at the end of each day to maintain food deprivation. Following habituation, mice were placed into a clear acrylic box with a narrow opening[31]. Food pellets were placed 1 cm away from the opening to the left of center, to encourage use of the right arm. Mice were acclimated and trained to reach for three to four days, and the mice that were readily reaching with the right paw were selected for experiments (~50–75% of mice). Mice were then trained for two weeks for 20 minutes or 20 successful reaches each day, whichever occurred first.

For three dimensional quantification of reaching kinematics, mice were placed in a reaching box with a modified pellet tray[31] in view of two high-speed, high-resolution monochrome cameras (HiSpec 1; 2 GB memory; Fastec) with 50 mm f/1.4 manual iris and focus lenses (C-Mount, 1/2 inch CCD; Fujinon) placed ~80° apart. An infrared LED light source (Clover Electronics) was mounted on top of each camera, and each lens was equipped with an infrared longpass filter (Midwest Optical Systems). Cameras were synced to each other, calibrated in space using MaxTRAQ 3D software (Innovision Systems) and set to 500 fps with a resolution of 1280 × 1024. A black background was used to increase contrast.

Mice were briefly anesthetized with isoflurane, and a 1.5 mm reflective hemisphere marker (B & L Engineering) was attached to the back of the right paw with adhesive. HiSpec camera control software was used to record reach trials, using an external trigger in ring mode. MaxTRAQ 2D software (Innovision Systems) was used to automatically track the marker and the pellet, with trials beginning as the paw left the ground and ending when the paw contacted the pellet, or when a full reach and prehension motion was completed. Tracked files were imported into MaxTRAQ 3D software to compute the coordinates of the marker and pellet in three dimensions.

Data were imported into MATLAB, low-pass filtered, and the starting points of reach trials were normalized by discarding reaches that started at a *z* distance (between paw and target) below 13 mm, and removing data frames for the remaining reaches above the 13 mm

threshold (post-normalization: 112 DTR reaches, 75 control reaches; see[31]). Analyses of early reach and late grab phases were performed before and after a distance-to-pellet threshold of 11 mm, where the paw passes through the opening of the box. Mean power spectra were calculated using a fast Fourier transform of individual reach velocities. Decay times were calculated by aligning all reaches within individual mice to the maximum velocity peak, averaging and normalizing, and fitting a single exponential function to the first three estimated peaks for each mouse. Power and decay analyses were performed on all reaches regardless of paw starting position, and thus non *z*-position normalized data were included (132 total reaches). To estimate the first and subsequent velocity peaks, the maximum velocity value was calculated for each reach in the first 50 ms, for the first peak, and the remainder of the reach, for the subsequent peak. Because all kinematic comparisons were performed within the same mouse before and after manipulation, and because tracking was automated, blinding was not performed. Analyses were performed on approximately equal numbers of male and female mice selected randomly from trained populations, and no sex-specific differences in reaching success or kinematics were identified.

Reach success was quantified over a period of 20 minutes or 20 hits, whichever came first, for 10–20 total days beginning after recovery from viral injection, and for 5–6 days post-DT (beginning 2 days after DT administration). Control mice were quantified for 14–24 days pre-DT and for 8–10 days post-DT (beginning ~one week after DT administration)[31].

Maximum digit abduction was calculated in MaxTRAQ 2D software by manually marking and measuring the distance between digits 2 and 4 in the frame captured by camera #1 in which the digits were maximally extended, as described[31]. The horizontal ladder task was performed as described[31,33]. Briefly, a high-definition camcorder (Canon Vixia HF11) was used to capture locomotion across a walkway consisting of 13 evenly-spaced rungs. An angled mirror below the walkway provided a bottom-up view of the rungs. The number of successful (hits) and unsuccessful (missteps) placements of the right and left forepaw were quantified for 10–15 full walks per mouse. The mean was calculated across all walks in individual mice pre- and post-DT. Pre-DT walks were recorded 1–2 weeks following viral injection and post-DT walks were recorded 5–7 days following DT administration.

For post-DT analysis of scratching mice were placed in a clear box and the amount of time spent scratching the right forelimb and the rate of scratching bouts over a 10 minute period were quantified. To prevent scratching-induced injury, mice were anesthetized with isoflurane and the claws of the right hindlimb were carefully removed with fine scissors. To block cutaneous excitation and evaluate the effects on scratching, reaching and ladder paw placement, a topical lidocaine cream (DermaPlanet; lidocaine, benzocaine, tetracaine) was applied to the right forearm and paw. Behavioral analysis resumed ~10–15 min after lidocaine application.

Joint model

We constructed a version of the Stein-Oguztöreli model[11] in which the angle of a single elbow-like joint (θ) is controlled by flexor (T_f) and extensor (T_e) muscle torques as follows,

$$\tau_m^2 \frac{d^2\theta}{dt^2} = T_e - T_f - k\tau_m \frac{d\theta}{dt} \quad (3)$$

The relationship between joint angle and the dimensionless flexor and extensor torque defined in Equation 3 is given by Newton's second law in its angular form (where net torque is proportional to angular acceleration) combined with a damping term scaled by a dimensionless parameter *k*. Timescales in the model are set by a muscle time constant τ_m, so that all variables and other parameters are dimensionless. We set the damping coefficient to $k = 0.5$, but found that our results were quite insensitive to the value of *k* (see below and Extended Data Fig. 8).

To initiate joint extension, an excitatory drive (I_e) that peaks at 25 ms is applied to the dimensionless extensor torque in the form of a Gaussian pulse,

$$I_e = 25\exp\left(-\frac{(t - 25\text{ms})^2}{2(10\text{ms})^2}\right) \quad (4)$$

The width and magnitude of this pulse determine the magnitude of initial joint extension and were set by eye to match the time course of forepaw extension found in the reaching data. To capture sensory feedback signals generated by changes in joint angle, we included an angular velocity dependent feedback term coupled with a gain scaling factor *h* that determines the efficacy with which sensory feedback drives flexor and extensor torques. This term, which is purely velocity dependent, introduces a drive of magnitude $s = h\tau_m d\theta/dt$ into the muscle torque, where *s* is the sensory feedback term. The relationship between extensor torque, the external excitatory drive, and the sensory feedback is given by

$$\tau_m^2 \frac{d^2T_e}{dt^2} + 2\tau_m \frac{dT_e}{dt} + T_e = I_e - h\tau_m \frac{d\theta}{dt} \quad (5)$$

which corresponds to an alpha-function muscle impulse response[11]. Here, the excitatory pulse I_e serves to increase extensor torque and the sensory feedback term increases extensor torque when the joint's angular velocity is less than zero, in other words when the joint angle is decreasing so the joint is flexing. Conversely, the relationship between flexor torque and sensory feedback is given by

$$\tau_m^2 \frac{d^2T_f}{dt^2} + 2\tau_m \frac{dT_f}{dt} + T_f = h\tau_m \frac{d\theta}{dt} \quad (6)$$

Here the sensory feedback activates the flexor torque when the joint's angular velocity is greater than zero, which occurs when the joint angle is increasing so the joint is extending. Note that there is no external drive to the flexor torque; its activation is achieved solely by sensory feedback.

In the original Stein-Orguztöreli model, sensory feedback depends on both a muscle length term (analogous to joint angle) and a change of muscle length term (analogous to joint angular velocity), and there is a sensory feedback delay. We found that it was not necessary to include a joint angle dependence to observe joint oscillation at high feedback gains and

so, for simplicity, we did not include these terms in our model. We also included feedback delays of varying latencies (Supplementary Note 5).

The model defined by equations 3, 5 and 6 has an instability when the gain h exceeds a critical value h_c that leads to ever-increasing oscillation amplitudes. We report all gains in relation to this critical gain h_c. To generate the traces included in Fig. 6c,d, we set sensory feedback gain at two different levels. For the low gain case, we set h to 10% of the critical gain ($h/h_c = 0.1$). Under this condition, the external extensor drive triggers joint extension, which is arrested by flexion activated by sensory feedback. The magnitude of the sensory feedback generates flexor torque of sufficient strength to arrest joint extension but of insufficient strength to generate further extensor torque. The velocity oscillation (Fig. 6c) is, in other words, near to being critically damped. In contrast, in the high gain case, where h is 60% of the critical gain ($h/h_c = 0.6$), the sensory activated flexor torque is of sufficient strength to activate an additional extensor torque, via a pronounced and rapid decrease in joint angle. This extensor torque, in turn, triggers an increase in joint angle of sufficient velocity to trigger another flexor torque and oscillation ensues (Fig. 6d). In the high gain case, to achieve continuous joint extension in the phase of oscillation we add a constant value to the extensor drive, setting $I_e \rightarrow I_e + 10$. We incorporated varying delays into the model by defining the contribution of the sensory feedback with a delayed angular velocity term such that for $t > t_{delay}$, $s(t) = h\tau_m \frac{d\theta}{dt}(t - t_{delay})$ where, in individual simulations, t_{delay} is taken from a set of delay values (1 ms, 3 ms, 5 ms, 10 ms) as reported in Extended Data Fig. 8. For multiple delays, we summed $\frac{d\theta}{dt}$ evaluated at different times, with equal weighting.

To simulate joint extension in the absence of subtractive scaling (representing postsynaptic inhibition) we added a constant value to the sensory feedback such that $s = h\tau_m \frac{d\theta}{dt} + C$. The added constant C represents the added feedback that would emerge in the absence of a tonic subtractive postsynaptic inhibitory term. We set $C = 0$ for $\frac{d\theta}{dt} \leq 0$. Without this rectification, the sensory feedback generates a constant flexing torque that destabilizes the resting state of the arm. We note that even in this case there is no oscillation in the joint, but in order to compare its behavior with reduced subtractive inhibition to cases without this added constant, we included the rectification step. We note that this is the only rectification in our model. In general, in order to keep the model linear, we did not sign-constrain either the stretch response or the muscle torques. We checked the behavior of the model with sign-constrained stretch responses and muscle torques and note that the basic oscillatory behavior persists at high gain, with near to critical-damping at low gain.

To analyze the oscillatory behavior of the model, we expressed the equations that describe the dynamics of the model (Equations 3, 5 and 6) as a system of five, first-order, linear differential equations:

$$\tau_m \frac{d}{dt}\begin{pmatrix} \tau_m \frac{d\theta}{dt} \\ T_e \\ T_f \\ z_e \\ z_f \end{pmatrix} = \begin{pmatrix} -k & 1 & -1 & 0 & 0 \\ 0 & -1 & 0 & 1 & 0 \\ 0 & 0 & -1 & 0 & 1 \\ -h & 0 & 0 & -1 & 0 \\ h & 0 & 0 & 0 & -1 \end{pmatrix} \begin{pmatrix} \tau_m \frac{d\theta}{dt} \\ T_e \\ T_f \\ z_e \\ z_f \end{pmatrix} \quad (7)$$

where z_e and z_f are variables that permit the two second-order Equations 5 and 6 to be expressed as four first-order equations. Computing the eigenvalues of the matrix describing this system of linear equations permits a description of the frequency and damping time of its dynamic modes. Three of the eigenvalues are real, corresponding to decaying modes. The eigenvalue with the least negative real part, which we call λ_1, is complex (actually it is one of a complex-conjugate pair of eigenvalues), corresponding to the dominant oscillatory mode of the model. The damping time of the oscillation is determined by the real part of λ_1 and the frequency f_{osc} of the oscillations by the imaginary part of λ_1. The damping describes the rate at which the oscillations decay. There is a level of the gain above which the damping time approaches infinity and oscillations do not decay, which defines the critical gain h_c.

To determine the appropriate values of the additional model parameters h and τ_m, we fit the oscillatory frequency and decay time of the leading eigenmode of the model to the values measured from post-DT reaching movements across mice (Supplementary Note 4). The frequency of oscillation of the model is

$$f_{osc} = \frac{|\mathrm{Im}(\lambda_1)|}{2\pi\tau_m} \quad (8)$$

where the numerator is the imaginary part of the complex eigenvalue corresponding to the model's oscillatory mode. The decay time of oscillation is,

$$\tau_{osc} = \frac{\tau_m}{|\mathrm{Re}(\lambda_1)|} \quad (9)$$

where the denominator is the real part of the complex eigenvalue corresponding to the model's oscillatory mode. The product of these two values generates a term n_{cycle} that is independent of the muscle time constant (the muscle time constant cancels when the right side of Equation 8 is multiplied by the right side of Equation 9),

$$n_{cycle} = \frac{|\mathrm{Im}(\lambda_1)|}{2\pi|\mathrm{Re}(\lambda_1)|} \quad (10)$$

Here n_{cycle} corresponds to the number of oscillatory cycles within a decay time constant. Since we have measured the frequency and decay time of post-DT oscillation, we calculated an experimentally derived value of n_{cycle}. We then used this value to determine which sensory gain level corresponds to the reach oscillations we observed. We also examined the extent to which the drag term k affects n_{cycle}, varying k across a 100-fold range and finding minimal change in the gain value that corresponds to our experimentally derived n_{cycle} value (Supplementary Note 4 and Extended Data Fig. 8). We then used this gain value to estimate

the muscle time constant (Supplementary Note 4 and Extended Data Fig. 8b). We found a biologically realistic value that was within the range used in the original model[11].

Antibodies

Primary antibodies: rabbit anti-GFP (1:500, Invitrogen); sheep anti-GFP (1:1000, AbD Serotec); rabbit anti-tdTomato (1:1000, Clontech; Living Colors DsRed); custom made guinea pig anti-vGluT1 (1:32,000), rabbit anti-GAD1 (1:10,000) and rabbit anti-GAD2 (1:10,000) were used as described previously[7]. Appropriate fluorophore-conjugated secondary antibodies were from the Jackson ImmunoReseach antibody series.

Immunohistochemistry and imaging

Mice were transcardially perfused with 4% paraformaldehyde 0.1M phosphate buffer fixative. For cryostat spinal cord sections, tissue was postfixed for 2 hours, washed, equilibrated in 30% sucrose 0.1M phosphate buffer solution, embedded and frozen in O.C.T. and sectioned along the axial plane at 20 μm onto glass slides. Immunohistochemistry was performed via exposure to primary antibodies (overnight at 4°C) and fluorophore-conjugated secondary antibodies (1 hour at room temperature). Sections were mounted using Fluoromount-G (SouthernBiotech) and coverslipped for imaging. Confocal images were taken with an LSM 710 microscope (Carl Zeiss).

Statistics

Results are expressed as the mean ± s.e.m. or s.d., as indicated. Electrophysiology data were analyzed using two-tailed paired *t* tests. For behavioral experiments early tests revealed very large effects of GABApre ablation (for example see Extended Data Table 1); power analysis demonstrated that with these effect sizes relatively small sample numbers are sufficient to achieve a power of value 0.8 with an alpha value of 0.05. The large effects observed mitigate potential confounds introduced by possible violations of parametric test assumptions. Reach success and kinematic data were analyzed using two-way repeated-measures ANOVA, enabling within-mouse pairing of data. Successful and unsuccessful reaches were grouped together for pre-DT conditions. There were no successful reaches following GABApre neuronal ablation in the kinematic assay. Bonferroni *post hoc* multiple comparisons tests were performed, as indicated. DT-treated control mice spared viral injection were analyzed in parallel experiments[31] and were used in two-way repeated-measures ANOVA analysis. For velocity power spectra analysis, lidocaine scratching analysis, digit abduction and ladder walk data, two-tailed paired *t* tests were used. $P < 0.05$ was considered significant.

Extended Data

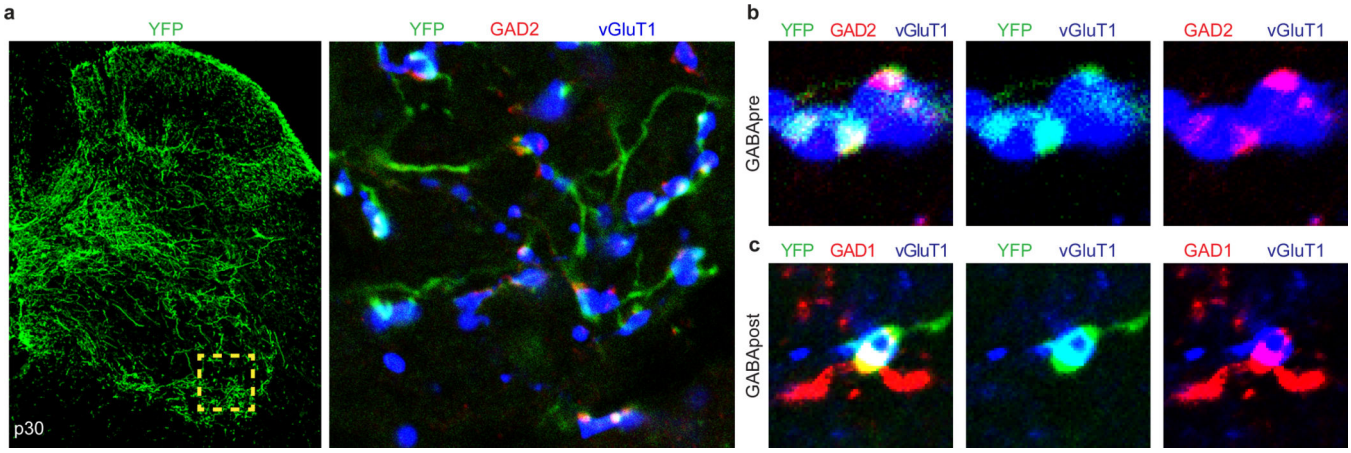

Extended Data Figure 1. Genetic targeting of GABApre neurons in lumbar spinal cord

a, At late ages (p30) *FLEX-ChR2-YFP* lumbar injection in *Gad2*^{Cre} mice marks GABApre neurons. In ventral horn (yellow box): YFP^{+}/GAD2^{+} GABApre boutons contact vGluT1^{+} proprioceptor terminals (**b,** high resolution); YFP^{OFF}/GAD1^{+} GABApost boutons do not contact vGluT1^{+} terminals. In contrast, a single YFP^{+}/GAD1^{+} bouton is in contact with a vGluT1^{+} terminal and is, therefore, a GABApre bouton. p30 injection marks GABApre boutons (75.8 ± 3.3%) but not GABApost boutons (0.99 ± 0.02%; n = 2). Values and error bars indicate mean ± s.e.m.

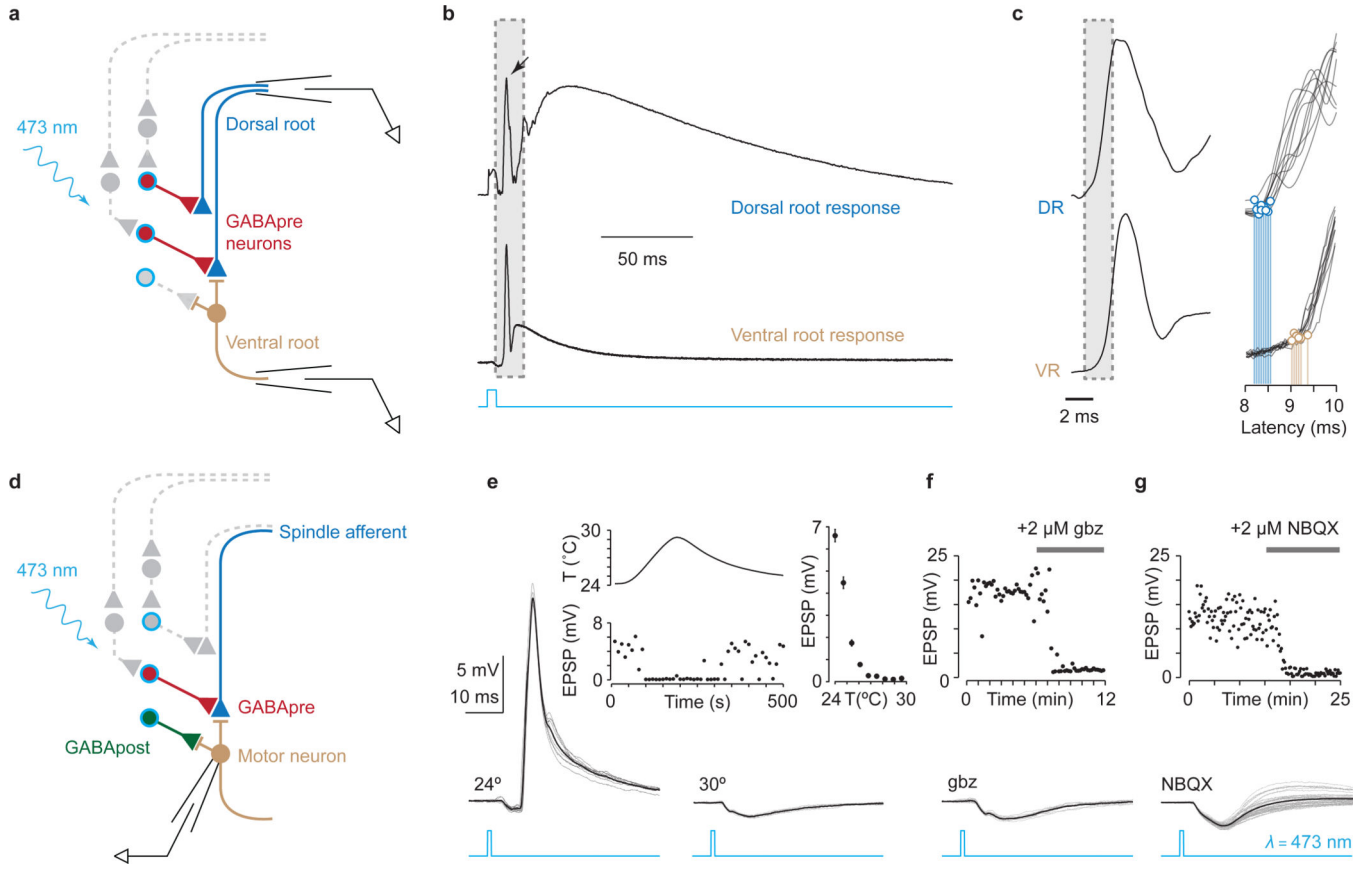

Extended Data Figure 2. Light-evoked excitation of spinal motor neurons reflects *Gad2*^{Cre} neuron-mediated proprioceptor depolarization

a, Recordings from dorsal and ventral roots during *Gad2*^{Cre} neuron photostimulation at 24–26°C. **b,** Light pulses induced primary afferent depolarization (top), accompanied by antidromic action potentials (black arrow), in dorsal roots shortly followed by orthodromic discharge in ventral roots (bottom). Outline indicates region shown in **c**. As shown in Fig. 2f, the time course and amplitude of PAD evoked by sensory stimulation and *Gad2*^{Cre}-neuron photostimulation are similar. Sensory-PAD: amplitude 203 ± 2 µV; 10%–90% rise time 18.8 ± 0.3 ms; 10%–90% decay time 275.7 ± 8.3 ms; n = 10 trials; *Gad2*^{Cre}-evoked PAD: amplitude 230 ± 1 µV; 10%–90% rise time 17.3 ± 0.3 ms; 10%–90% decay time 186.6 ± 2.0 ms. **c,** Mean antidromic spike recorded in dorsal root (top) and orthodromic spike recorded in ventral root (bottom). The latencies of spike onset (outlined region) are shown on the right (dorsal root spike onsets, blue circles; ventral root spike onsets, brown circles; vertical lines, latencies from light pulse onset). Ventral root spike onset was consistently later than dorsal root spike onset (mean delay 0.73 ± 0.03 ms; mean dorsal root spike latency 8.01 ± 0.42 ms; mean ventral root spike latency 8.74 ± 0.40 ms; two-tailed paired t test, $P < 0.05$, n = 2 preparations), indicating that light-evoked spikes occur in sensory neurons prior to motor neurons. **d,** Whole-cell patch-clamp recording from spinal motor neurons during *Gad2*^{Cre} neuron photoactivation. **e,** Light-induced EPSPs (1 ms pulses) evoked at 24° (left) but not 30°C (right). Inset, left, temperature dependence of light-evoked EPSPs (top plot, bath temperature; bottom plot, EPSP amplitudes; both plotted as

functions of time). Inset, right, average EPSP amplitude as a function of bath temperature. **f,** During low temperature (24–26°C) recording conditions, application of the GABA-A receptor antagonist gabazine (SR 95531, gbz, 2 μM) abolishes light-evoked EPSPs but leaves the glycinergic light-evoked IPSP intact. Inset, individual light-evoked EPSP amplitudes during gabazine application (grey bar). **g,** During low temperature (24–26°) recording conditions, application of the AMPA-receptor antagonist NBQX (2 μM) abolishes the fast, high-amplitude component of the light-evoked EPSP but does not affect the light-evoked IPSP. Inset, individual EPSP amplitudes during NBQX application (grey bar). Together these experiments are consistent with the view that synchronous activation of *Gad2*^{Cre} neurons at low temperature depolarizes sensory afferent terminals with sufficient strength to generate sensory action potentials and subsequent glutamate release, in turn activating motor neurons (Supplementary Note 2). Values and error bars indicate mean ± s.e.m.

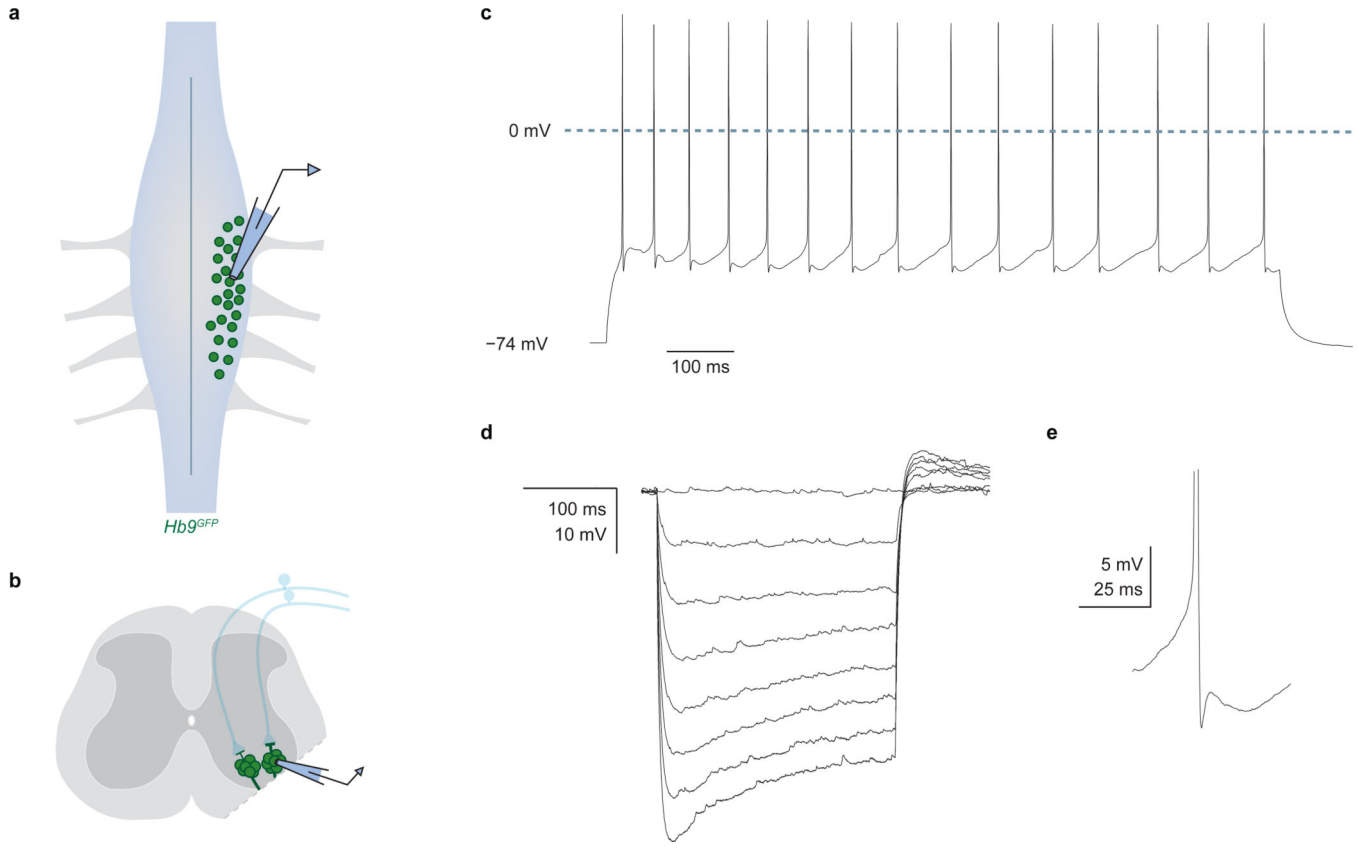

Extended Data Figure 3. Physiological identification of spinal motor neurons

a, Whole-cell patch-clamp recording from spinal motor neurons in a whole (or hemisected) cord, in which motor neurons were targeted via visual guidance using GFP expression in *Hb9*^{GFP} mice. **b,** Removal of the ventral-lateral white matter permits visual identification and access to spinal motor neurons without disrupting sensory-motor or interneuron circuitry. **c–e,** Motor neurons recorded in this configuration exhibit physiological properties typically associated with spinal motor neurons[56]: **c,** current injection elicits repetitive action potentials, with rate adaptation; **d,** hyperpolarizing current steps reveal membrane potential

sag, indicative of I_h current; and **e,** the waveform of motor neuron action potentials exhibits an early hyperpolarization indicative of an I_A current and a prolonged hyperpolarization likely mediated by a calcium-activated $I_{K(Ca)}$ current.

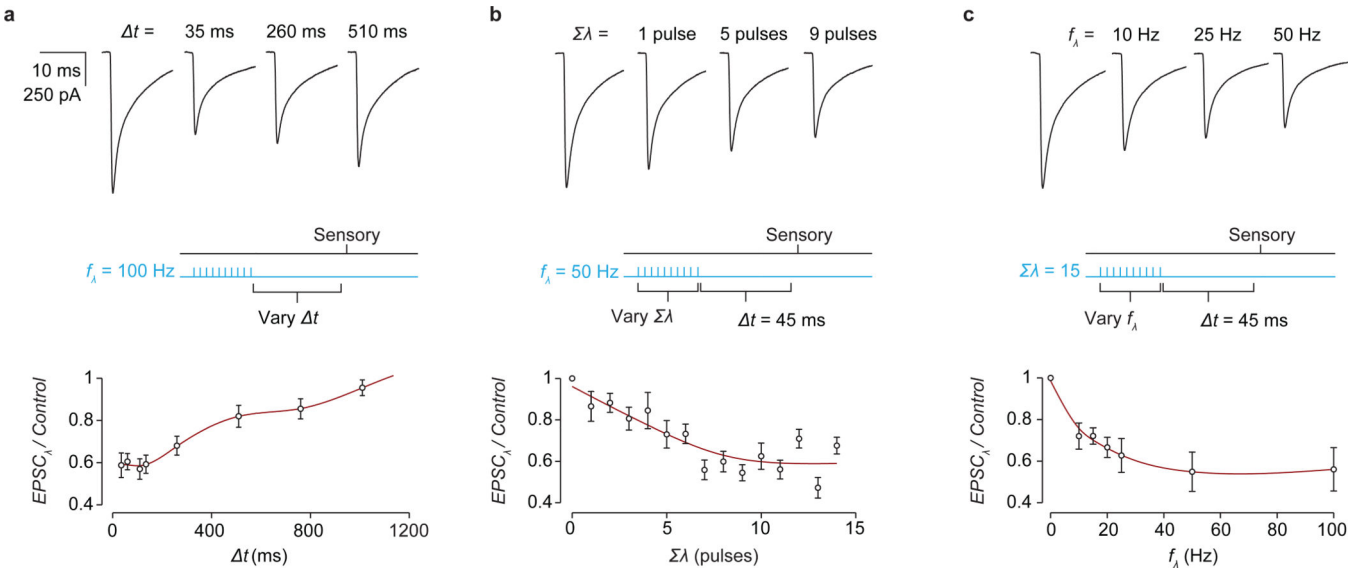

Extended Data Figure 4. *Gad2*^{Cre} neuron photoactivation scales sensory EPSC amplitude

a, Sensory-evoked EPSCs evoked in motor neurons at varying delays (Δ*t*) between the cessation of photostimulation (ten 1 ms pulses, 100 Hz, blue line) and sensory stimulation (black line). Fractional EPSC amplitude (*EPSC*$_\lambda$/*Control*) plotted as a function of sensory delay Δ*t*. Maximal EPSC suppression was seen at the smallest Δ*t* values. Plot depicts fractional EPSC amplitude for Δ*t* = 35, 60, 110, 135, 260, 510, 760 and 1010 ms. **b,** Sensory-evoked EPSCs following a varying number of light pulses (Σλ, blue line) at a fixed latency (Δ*t* = 45 ms) recruits *Gad2*^{Cre} neuron-evoked EPSC suppression of increasing magnitude. Plot depicts fractional EPSC amplitude for Σλ = 1–14 pulses. **c,** Sensory-evoked EPSCs following varying *Gad2*^{Cre} neuron photoactivation frequency (f_λ, blue line) at a fixed sensory delay (Δ*t* = 45 ms) recruits increasing suppression of sensory-EPSCs. Plot depicts fractional EPSC amplitude for f_λ = 10, 15, 20, 25, 50 and 100 Hz. These data, along with the linear scaling of *Gad2*^{Cre} neuron firing with photoactivation frequency (Fig. 2d), indicate that the graded suppression of sensory-EPSCs is a consequence of increased spiking in *Gad2*^{Cre} neurons. Red curves indicate splines fit to the data. Error bars indicate mean ± s.d. We note that these experiments require effective control of *Gad2*^{Cre} neuronal spiking. As shown in Fig. 2b–d, light pulses induced pronounced currents and reliable spiking in ChR2-YFP$^+$ *Gad2*^{Cre} neurons ($V_{holding}$ −60 mV; peak 773 ± 268 pAmp; steady state 537 ± 193 pAmp; 10%–90% rise time 2.1 ± 0.4 ms; 10%–90% decay time 33.5 ± 4.3 ms; *n* = 3)[20]. Values indicate mean ± s.e.m.

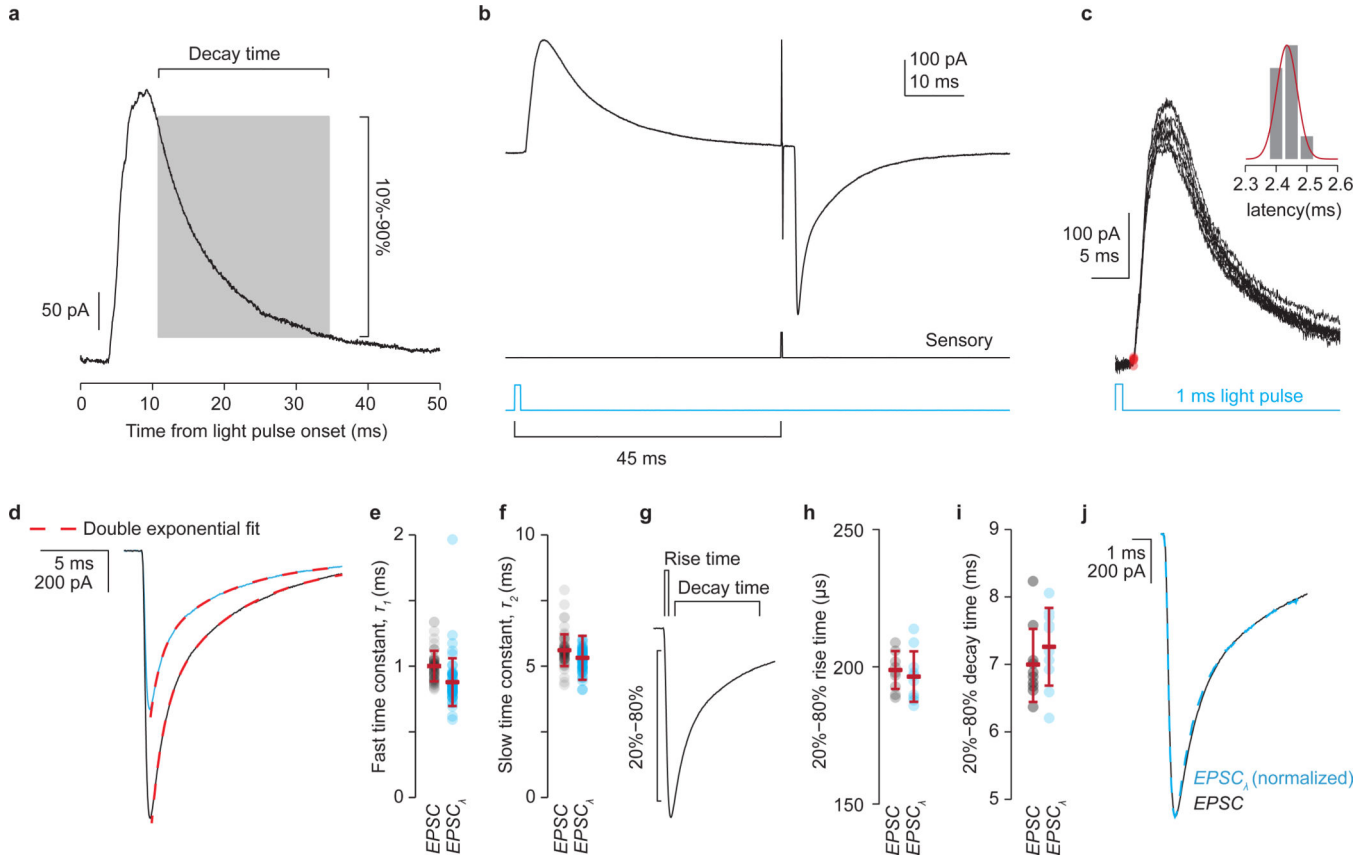

Extended Data Figure 5. Postsynaptic inhibition cannot account for the observed reduction in sensory-evoked EPSC amplitude

a, Motor neuron IPSC elicited by a 1 ms light pulse. IPSCs had a 10%–90% decay time of 23.7 ± 1.9 ms and a mean peak amplitude of 299 ± 20 pAmp at −60 mV holding potential (n = 9). IPSCs reversed at ~−65 mV (Nernst equation predicts E_{Cl} = −67.5 mV). **b,** A 45 ms delay between the light pulse (blue) and electrical sensory stimulation pulse (black) permits the GABApost-mediated IPSC to decay almost completely before sensory-EPSC onset. **c,** *Gad2*^{Cre} neuron-evoked IPSCs are monosynaptic. Red circles indicate estimated onset times with distribution of individual IPSC latencies shown in inset. Mean IPSC onset latency 2.4 ± 0.3 ms; cv_{onset} 0.03 ± 0.007; n = 5. As shown in Fig. 3b–d, IPSCs are almost completely blocked by strychnine (str), with only limited effects of GABA receptor antagonists (gbz/cgp). IPSC index, ratio of IPSC amplitude with drug to control IPSC (str 0.09 ± 0.02, two-tailed paired t test, $P < 10^{-5}$, n = 5; gbz/cgp 0.82 ± 0.04, $P < 0.05$, n = 3). Moreover, as shown in Fig. 3e,f, the *Gad2*^{Cre} neuron-evoked suppression of sensory-evoked EPSCs is unaffected by strychnine (str) but abolished by co-application of the GABA-A and -B receptor antagonists SR 95531 and CGP54626. (EPSC index, drug has no effect = 1; drug abolishes EPSC-suppression = 0; str 1.04 ± 0.02, two-tailed paired t test, P = 0.3, n = 3; gbz/cgp 0.02 ± 0.03, two-tailed paired t test, $P < 0.02$, n = 4; see Methods). **d,** Sensory-evoked *EPSC* (black trace, control) and $EPSC_\lambda$ (blue trace, with *Gad2*^{Cre} photoactivation) waveforms fit with double exponential function ($EPSC_{fit}$, dashed lines, red) of the form $EPSC_{fit}(t) = A1 \exp(-t/\tau_1) + A2 \exp(-t/\tau_2)$. **e,** Distribution of the fast decay time constant (τ_1) is similar for *EPSC* (black circles) and $EPSC_\lambda$ (blue circles) waveforms (*EPSC* mean τ_1

96 ± 13 μs; $EPSC_{\lambda}$ τ_1 89 ± 14 μs; n = 100 trials). **f,** Distribution of the slow decay time constant (τ_2) is similar for *EPSC* and $EPSC_{\lambda}$ waveforms (*EPSC* mean τ_2 5.56 ± 0.41 ms; $EPSC_{\lambda}$ τ_2 5.41 ± 0.48 ms). **g,** Estimation of the 20%–80% rise and decay time provides an independent measure of EPSC kinetics. **h,** The 20–80% rise time for control EPSCs (*EPSC* 199 ± 7 μs) and that of EPSCs evoked following photoactivation ($EPSC_{\lambda}$ 197 ± 9 μs). **i,** The 20%–80% decay time for control EPSCs (*EPSC* 7.0 ± 0.5 ms) and that of EPSCs evoked following photoactivation ($EPSC_{\lambda}$ 7.3 ± 0.6 ms). **j,** Normalization of the light-conditioned $EPSC_{\lambda}$ waveform to the unconditioned *EPSC* waveform permits estimation of waveform correlation as a further metric of the similarity of the two waveforms (Pearson's correlation, $R > 0.999$, $P < 0.0001$). The unaltered time course of the EPSC waveform argues against light-evoked EPSC suppression mediated by a postsynaptic inhibitory conductance. Although in theory a postsynaptic inhibitory conductance should have no effect on the current waveform of a perfectly clamped EPSC, the large size and low input resistance of the motor neurons, as well as the dendritic nature of the majority of sensory inputs, makes it likely that the voltage clamp is insufficient to prevent some depolarization of the dendrites, which would be altered via inhibitory conductance. In support of this idea the time course of EPSP waveforms recorded in current clamp are unaltered by photoactivation of $Gad2^{Cre}$ neurons under the conditions described here (data not shown). Values and error bars indicate mean ± s.d.

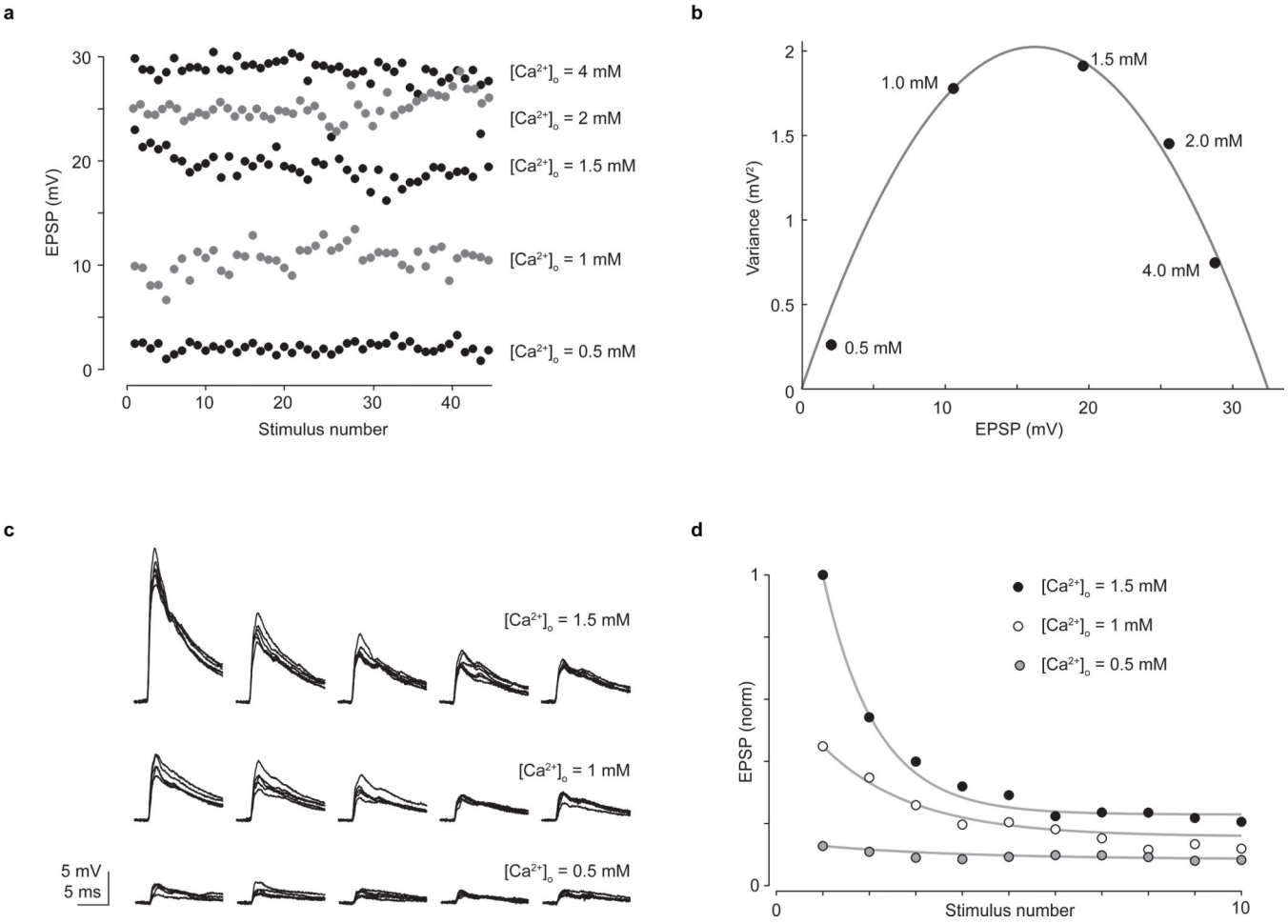

Extended Data Figure 6. Estimation of release probability using mean variance analysis validates the short-term depression model

a, Amplitudes of 225 EPSPs recorded from a spinal motor neuron evoked by sensory stimulation across five calcium concentrations (0.5 mM, 1.0 mM, 1.5 mM, 2.0 mM and 4.0 mM) exhibiting fluctuating amplitudes due to calcium-controlled changes in transmitter release probability. EPSPs were recorded at each calcium concentration (0.1 Hz sensory stimulation frequency) once EPSP amplitude had settled to a steady value. Each calcium concentration was visited twice in sequence per recording. Data were collected in current clamp to reduce possible confounds due to changes in series resistance over the long recordings required to collect the data. **b,** EPSP variance versus amplitude (black circles) is well fit by a quadratic function[55] (grey line) of the form $\sigma^2 = A\mu + B\mu^2$, where σ^2 is the variance across EPSPs and μ is the mean EPSP amplitude for each calcium condition. The release probability (p_{rel}) is given by $p_{rel} = \mu\,(B/A)\,(1+cv_q^2)$ where cv_q is the coefficient of variation in EPSP amplitude from a single release site. We set $cv_q = 0.3$, following accepted values[55]. Using this method, we found that for the representative neuron shown here p_{rel} = 0.97, 0.86, 0.66, 0.35 and 0.07 for $[Ca^{2+}]_o$ = 4 mM, 2 mM, 1.5 mM, 1 mM and 0.5 mM, respectively. **c,** At each calcium concentration EPSP depression was monitored via repetitive stimulation of the dorsal root (10 pulses, 10 Hz). Shown here are five consecutive EPSPs for three calcium concentrations (1.5 mM, 1.0 mM and 0.5 mM; superposition of ten trials). **d,**

Changes in EPSP depression as a function of calcium concentration were quantified using a model of short-term depression[29,54] (see Fig. 3h–j). The short-term depression model was set to generate EPSP amplitudes that depressed at different rates because of changes to the release probability term of the model. These EPSP amplitudes were fit by exponential functions. Normalized mean EPSP amplitudes at different calcium concentrations (circles) were then superimposed upon the curves generated by the short-term depression model (grey lines). The depression shown here is captured by setting the release probability parameters in the model to 0.52, 0.30 and 0.07 for $[Ca^{2+}]_o$ = 1.5 mM, 1.0 mM and 0.5 mM respectively, which are in good correspondence with the release probability terms estimated using mean-variance analysis. For $[Ca^{2+}]_o$ > 1.5 mM the short-term depression model consistently produced lower estimates for release probability than the mean variance analysis. But the correspondence at 1.5 mM and below argues for the short-term depression model being an effective means of capturing changes in release probability at sensory-motor synapses.

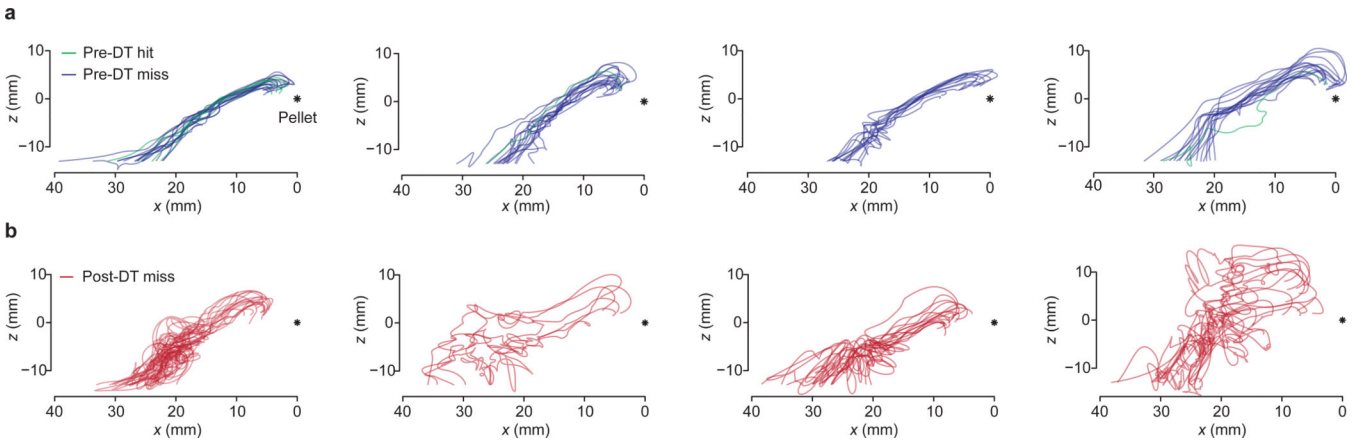

Extended Data Figure 7. Reach trajectories before and after ablation of GABApre neurons

a, Pre-DT reach trajectories for four mice. Two dimensional paw trajectories were generated by projecting the three dimensional trajectory into the *x*-*z* plane. Green traces represent pre-DT hits, blue traces pre-DT misses. The asterisk indicates the location of the target food pellet. **b,** Post-DT two dimensional reach trajectories for the same mice, red traces. These mice were used for all kinematic quantification included in Extended Data Table 1.

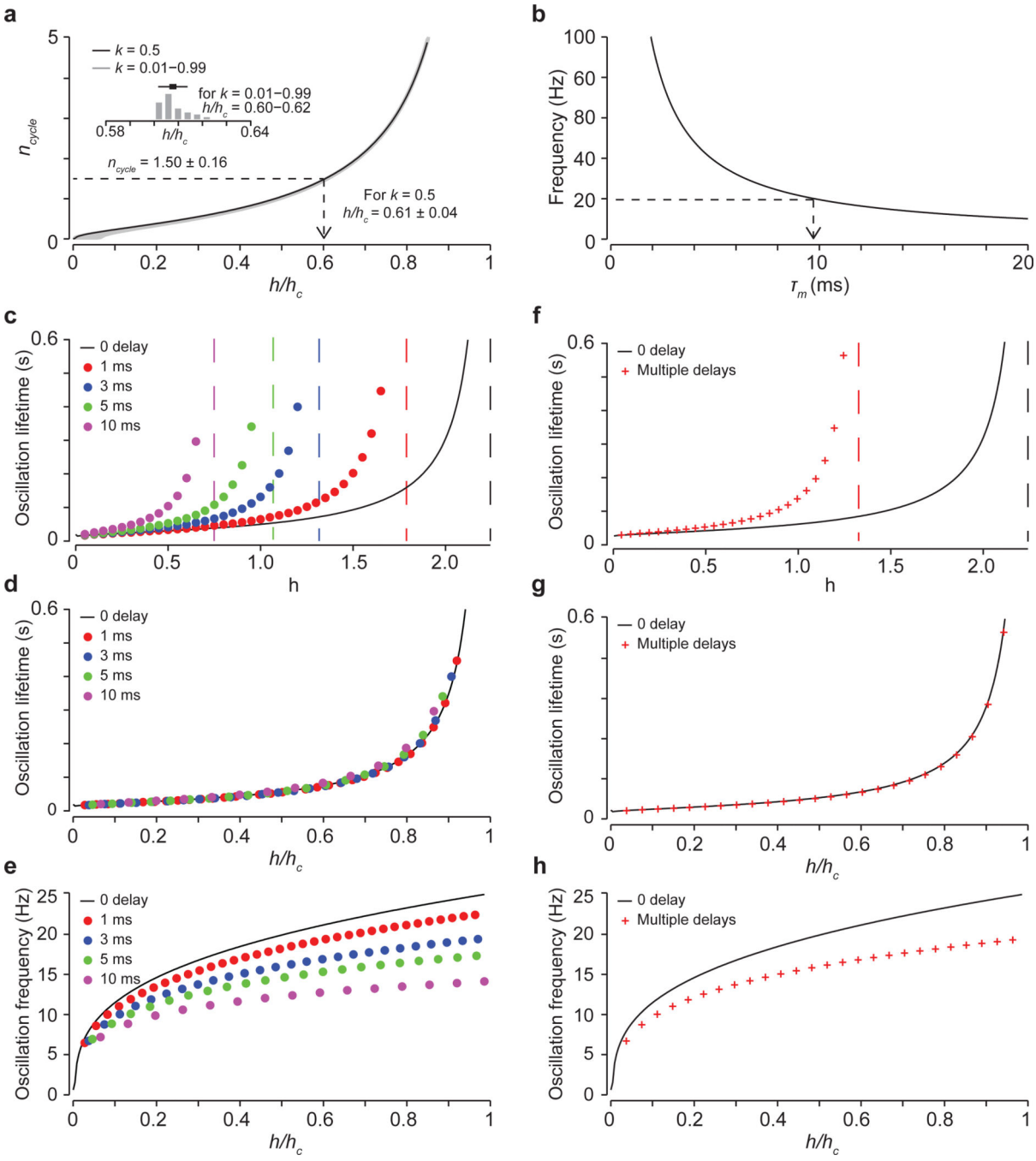

Extended Data Figure 8. Fitting the model to the frequency and decay time of post-DT reach velocity oscillations

a, To fit the model parameters to the experimentally derived frequency and decay times, we took advantage of the fact that the product of the oscillatory frequency and decay time ($f_{osc}\tau_{osc}$) creates a parameter free value n_{cycle}, which does not depend on the muscle time constant. The term n_{cycle} corresponds to the number of oscillatory cycles per decay time constant and scales as a function of feedback gain. Plotting n_{cycle} as a function of feedback gain (h/h_c, where h_c is the critical gain above which oscillations do not decay) permits

estimation of the gain value that corresponds to the experimentally derived value of n_{cycle}. Importantly, the corresponding gain value does not depend on the drag parameter k (inset and grey shading beneath black curve). Varying k by 100-fold results in minimal changes in the corresponding gain, with h/h_c varying from 0.6 to 0.62. The grey curves represent the relationship between n_{cycle} and h/h_c across the full range of k values. Arrow indicates the gain value corresponding to the experimentally derived vale of n_{cycle} for $k = 0.5$. See Supplementary Note 4 and Methods. **b,** To estimate the appropriate muscle time constant, we used the five dimensional matrix that defines the model (see Methods) to calculate the imaginary part of the complex eigenvalue corresponding to $k = 0.5$ and $h/h_c = 0.61$. We found a time constant of $\tau_m = 9.6$ ms (indicated by the arrow), which is within the range used in the original model[11] based on experimentally-derived values[57]. **c,** Introduction of delays in the feedback loop does not alter the basic properties of the model. Oscillation lifetime (τ_{osc}) as a function of absolute gain h for delays of 1 ms, 3 ms, 5 ms and 10 ms as compared to no delay (black trace). The vertical dashed lines indicate the gain level above which oscillations never decay (the critical gain, h_c) for each delay value. **d,** Scaling these curves by their corresponding critical gain values reveals equivalent oscillatory lifetimes (h/h_c). **e,** Oscillation frequency (f_{osc}) as a function of normalized gain. As feedback delays increase, peak oscillatory frequency decreases. For higher delay conditions, where the oscillation frequency is significantly below 20 Hz, decreasing the muscle time constant results in higher oscillation frequencies. Thus for longer delays ~20 Hz oscillation is possible, but requires an increasingly small muscle time constant. **f–h** are as **c–e** but with three simultaneous loops of different delays (1 ms, 3 ms and 5 ms). In the presence of multiple simultaneous feedback delays the model continues to oscillate at a single dominant peak frequency for a given gain level. See Supplementary Note 5.

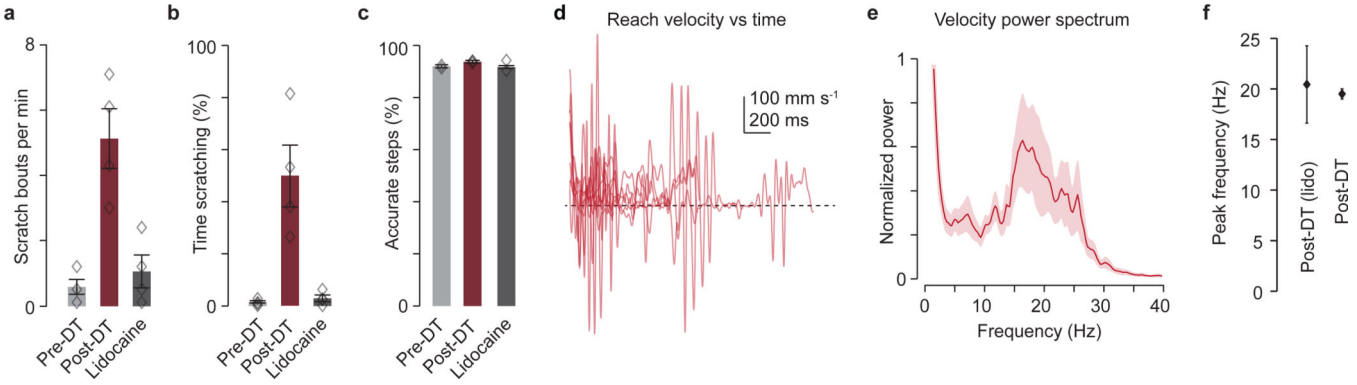

Extended Data Figure 9. Lidocaine application abolishes scratching behavior but not reach oscillations, and does not affect forepaw stepping behavior

a, Scratching behavior increased following GABApre neuronal ablation, but was reduced to normal levels by topical application of lidocaine to the right forearm and paw. The rate of scratching bouts per 10 minute observation session increased following DT-administration, but returned to normal levels following lidocaine application (mean rate of scratch bouts per minute: pre-DT 0.6 ± 0.2 min^{-1}; post-DT 5.1 ± 0.9 min^{-1}; post-DT plus lidocaine 1.0 ± 0.5 min^{-1}; pre-DT versus post-DT, $P < 0.05$; post-DT versus post-DT + lidocaine, $P < 0.05$, $n = 4$). **b,** Similarly, the percent time spent scratching during a 10 minute observation period is

normally low (pre-DT 1.6 ± 0.4%) but increased following DT-administration (post-DT 49.8 ± 11.7%) and trended toward baseline after lidocaine application (post-DT plus lidocaine 2.9 ± 1.3%). Pre-DT versus post-DT, two-tailed paired *t* test, $P < 0.05$; post-DT versus post-DT + lidocaine, $P = 0.06$, $n = 4$. **c,** Stepping success rate on the horizontal ladder task[33]. Lidocaine did not affect stepping performance (pre-DT 90 ± 1%; post-DT 93 ± 1%; post-DT + lidocaine 92 ± 1%; two-tailed paired *t* test; pre-DT versus post-DT, $P = 0.7$; post-DT versus post-DT + lidocaine, $P = 0.6$, $n = 3$). The equivalent rate of accuracy across conditions indicates that lidocaine application has no overt effect on forepaw placement during stepping. As shown in Fig. 4f, right and left forepaw placement accuracy pre-DT versus post-DT were similar (right paw: pre-DT 90.2 ± 2.0%; post-DT 79.6 ± 13.2%; two-tailed paired *t* test, $P = 0.41$; left paw: pre-DT 80.8 ± 2.7%; post-DT 76.1 ± 6.9%; two-tailed paired *t* test, $P = 0.34$, $n = 4$.) In contrast to stepping accuracy, as shown in Fig. 4e, reach success degraded following GABApre ablation as compared to control mice[31] (pre-DT 48.6 ± 3.7%; post-DT 4.9 ± 4.7%; two-way repeated-measures ANOVA, interaction of group × toxin: $F_{1,6} = 17.64$, $P = 0.006$; *post-hoc* Bonferroni test, DTR: $P < 0.01$, $n = 4$ DTR, $n = 4$ control). **d,** Post-DT velocities of individual reaches continued to exhibit oscillation following topical lidocaine application. **e,** Power spectrum of post-DT reaches following lidocaine application ($n = 2$ mice, 14 reaches; shaded area, s.d.). **f,** Mean dominant frequency peak for post-DT reaches with lidocaine (20.5 ± 3.8 Hz) and without lidocaine (19.5 ± 0.5 Hz; see Fig. 5f,g). The persistence of limb oscillation during lidocaine block implicates a loss of proprioceptive rather than cutaneous presynaptic inhibition as the origin of the oscillation uncovered by GABApre neuronal ablation. Values and error bars indicate mean ± s.e.m.

Extended Data Table 1
Reaching kinematics after GABApre neuronal ablation

The following kinematic parameters were perturbed in the reach, but not the grab, phase in GABApre ablated relative to control mice[31]: mean number of forepaw direction reversals towards and away from the pellet (n = 4 DTR mice, 112 reaches, n = 4 control mice, 75 reaches; two-way repeated-measures ANOVA, interaction of group × condition, reach phase: $F_{1,6}$ = 15.48, P = 0.01; *post-hoc* Bonferroni test, DTR pre-DT versus post-DT, P < 0.001; grab phase: $F_{1,6}$ = 3.24, P = 0.12); mean number of high velocity (>100 mm s^{-1}) reversals of paw direction (reach phase: $F_{1,6}$ = 35.04, P = 0.001; *post-hoc* Bonferroni test, DTR pre-DT versus. post-DT, P < 0.001; grab phase: $F_{1,6}$ = 2.71, P = 0.15); mean s.d. of paw distance to target (reach phase: $F_{1,6}$ = 8.57, P = 0.03; grab phase: $F_{1,6}$ = 0.60, P = 0.47); mean s.d. of paw velocity (reach phase: $F_{1,6}$ = 25.55, P = 0.002; *post-hoc* Bonferroni test, DTR pre-DT versus post-DT, P < 0.01; grab phase: $F_{1,6}$ = 1.12, P = 0.33); the mean total distance travelled by the paw (reach phase *increase* in distance travelled: $F_{1,6}$ = 62.42, P = 0.0002; *post-hoc* Bonferroni test, DTR pre-DT versus post-DT, P < 0.0001; grab phase *decrease* in distance travelled: $F_{1,6}$ = 15.57, P = 0.01; *post-hoc* Bonferroni test, DTR pre-DT versus post-DT, P < 0.01); and mean movement duration (reach phase *increase* in duration: $F_{1,6}$ = 12.67, P = 0.01; *post-hoc* Bonferroni test, DTR pre-DT versus post-DT, P < 0.01; grab phase *decrease* in duration: $F_{1,6}$ = 13.14, P = 0.01; *post-hoc* Bonferroni test, DTR pre-DT versus post-DT, P < 0.01). Mean reach speed did not differ significantly between conditions. Digit abduction (maximum distance between digits 2 and 4) during grasp attempts was unaffected by GABApre neuronal ablation (pre-DT, 3.38 ± 0.25 mm; post-DT, 3.39 ± 0.24 mm; two-tailed paired t test, P = 0.98, n = 5). Reaching kinematics were not affected during any phase of movement in DT-treated control mice that did not receive *FLEX-DTR-GFP*[31].

	Reach phase		Grab phase	
	Pre-DT	**Post-DT**	**Pre-DT**	**Post-DT**
Direction reversals (no.)	1.38 ± 0.30	13.36 ± 1.36	1.72 ± 0.12	1.18 ± 0.08
Direction reversals at >100 mm s^{-1} (no.)	0.07 ± 0.02	5.68 ± 0.46	0.02 ± 0.01	0.10 ± 0.03
s.d. of distance to target (mm)	2.93 ± 0.24	4.89 ± 0.25	0.91 ± 0.09	0.92 ± 0.05
s.d. of velocity (mm s^{-1})	36.34 ± 1.80	92.05 ± 6.80	35.20 ± 2.10	48.11 ± 2.24
Total distance travelled per reach (mm)	26.87 ± 0.44	84.67 ± 3.14	12.63 ± 0.40	8.03 ± 0.31
Total duration per reach (ms)	255.20 ± 7.84	582.93 ± 47.24	116.47 ± 6.80	65.78 ± 3.96
Mean reach speed (mm s^{-1})	113.79 ± 5.80	157.99 ± 12.03	106.83 ± 4.27	133.25 ± 5.64

	Entire reach	
	Pre-DT	**Post-DT**
Initial peak velocity at <50 ms (mm s^{-1})	296.96 ± 16.73	284.14 ± 50.61
Subsequent peak velocity at >50 ms (mm s^{-1})	161.80 ± 10.36	274.17 ± 29.06
Peak power (18–22 Hz)	143 ± 37	957 ± 270

As shown in Fig. 5d,e the amplitude of the first velocity peak (within the first 50 ms of the reach) did not differ between pre-DT and post-DT reaches, while the subsequent peak velocity (>50 ms from reach initiation) was significantly higher

for post-DT reaches (initial peak: pre-DT versus post-DT, two-tailed paired *t* test, $P = 0.82$; subsequent peak: pre-DT versus post-DT, two-tailed paired *t* test, $P = 0.04$, $n = 4$ mice, 112 reaches). As shown in Fig. 5g, peak power in the 18–22 Hz frequency band was significantly higher in post-DT mice (two-tailed paired *t* test, $P < 0.02$, $n = 5$ mice, 132 reaches; see Methods). Successful and unsuccessful pre-DT reaches were grouped together for all analysis. There were no post-DT successful reaches in the kinematic assay. Values indicate mean ± s.e.m.

Supplementary Material

Refer to Web version on PubMed Central for supplementary material.

Acknowledgements

We are grateful to K. Miao for assistance with mouse genotyping; M. Mendelsohn, N. Zabello and S. Patruni for animal care; and B. Han, K. MacArthur, S. Morton and I. Schieren for technical assistance. We thank G.Z. Mentis for the custom built recording stage used in the electrophysiology experiments; K. Deisseroth for the *AAV-FLEX-hChR2-YFP* plasmid; and M. Churchland for providing a low-pass filter. We are grateful to C.E. Schoonover for sustained encouragement, engagement and discussion; B. Babadi for assistance in implementing the short-term depression model; the instructors of the Ion Channel Physiology course at Cold Spring Harbor Laboratory for guidance; and S. Siegelbaum and A. Losonczy for advice on electrophysiology. We thank R. Axel, S. Druckmann, C. Jahr, A. Karpova, A. Miri, K. Seki, and S. Siegelbaum for valuable discussion and comments on the manuscript. E.A. is a Howard Hughes Medical Institute Fellow of the Helen Hay Whitney Foundation; J.Z.H. was supported by NIH grant MH078844; L.F.A. was supported by NIH grant MH093338 and by the Harold and Leila Y. Mathers, Gatsby and Swartz Foundations; T.M.J was supported by NIH grant NS033245, the Harold and Leila Y. Mathers Foundation and Project A.L.S., and is an investigator of the Howard Hughes Medical Institute.

References

1. Windhorst U. Muscle proprioceptive feedback and spinal networks. Brain Research Bulletin. 2007; 73:155–202. [PubMed: 17562384]
2. Arber S. Motor circuits in action: specification, connectivity, and function. Neuron. 2012; 74:975–989. [PubMed: 22726829]
3. Frank K, Fuortes M. Presynaptic and postsynaptic inhibition of monosynaptic reflexes. Federation Proceedings. 1957; 16:49–50.
4. Eccles JC, Eccles RM, Magni F. Central inhibitory action attributable to presynaptic depolarization produced by muscle afferent volleys. Journal of Physiology. 1961; 159:147–166. [PubMed: 13889050]
5. Lundberg A. Supraspinal control of transmission in reflex paths to motoneurones and primary afferents. Progress in Brain Research. 1964; 12:197–221. [PubMed: 14202439]
6. Rudomin P, Schmidt RF. Presynaptic inhibition in the vertebrate spinal cord revisited. Experimental Brain Research. 1999; 129:1–37. [PubMed: 10550500]
7. Betley JN, et al. Stringent specificity in the construction of a GABAergic presynaptic inhibitory circuit. Cell. 2009; 139:161–174. [PubMed: 19804761]
8. Conradi S. Ultrastructure of dorsal root boutons on lumbosacral motoneurons of the adult cat, as revealed by dorsal root section. Acta Physiologica Scandinavica. 1969; 332(Supplementum):85–115.
9. Rossignol S, Dubuc R, Gossard J-P. Dynamic sensorimotor interactions in locomotion. Physiological Reviews. 2006; 86:89–154. [PubMed: 16371596]
10. Akay, T.; Tourtellotte, WG.; Arber, S.; Jessell, TM. Program No. 782.19. 2013 Neuroscience Meeting Planner. San Diego, CA: Society for Neuroscience; 2013. Locomotor pattern degrades in absence of proprioceptive feedback: A genetic, physiological, and behavioral analysis. Online.
11. Stein RB, Oğuztöreli MN. Tremor and other oscillations in neuromuscular systems. Biological Cybernetics. 1976; 22:147–157. [PubMed: 1276248]
12. Capaday C, Stein RB. A method for simulating the reflex output of a motoneuron pool. Journal of Neuroscience Methods. 1987; 21:91–104. [PubMed: 3682884]
13. Capaday C, Stein RB. Difference in the amplitude of the human soleus H reflex during walking and running. Journal of Physiology. 1987; 392:513–522. [PubMed: 3446790]

14. Capaday C. A re-examination of the possibility of controlling the firing rate gain of neurons by balancing excitatory and inhibitory conductances. Experimental Brain Research. 2002; 143:67–77. [PubMed: 11907692]
15. Hughes DI, et al. P boutons in lamina IX of the rodent spinal cord express high levels of glutamic acid decarboxylase-65 and originate from cells in deep medial dorsal horn. Proceedings of the National Academy of Sciences. 2005; 102:9038–9043.
16. Soghomonian J-J, Martin DL. Two isoforms of glutamate decarboxylase: why? Trends in Pharmacological Sciences. 1998; 19:500–505. [PubMed: 9871412]
17. Taniguchi H, et al. A resource of Cre driver lines for genetic targeting of GABAergic neurons in cerebral cortex. Neuron. 2011; 71:995–1013. [PubMed: 21943598]
18. Sonner PM, Ladle DR. Early postnatal development of GABAergic presynaptic inhibition of Ia proprioceptive afferent connections in mouse spinal cord. Journal of Neurophysiology. 2013; 109:2118–2128. [PubMed: 23343895]
19. Behar T, et al. Many spinal cord cells transiently express low molecular weight forms of glutamic acid decarboxylase during embryonic development. Developmental Brain Research. 1993; 72:203–218. [PubMed: 8485844]
20. Zhang F, Wang L-P, Boyden ES, Deisseroth K. Channelrhodopsin-2 and optical control of excitable cells. Nature Methods. 2006; 3:785–792. [PubMed: 16990810]
21. Willis J, W D. Dorsal root potentials and dorsal root reflexes: a double-edged sword. Experimental Brain Research. 1999; 124:395–421. [PubMed: 10090653]
22. Barker JL, Nicoll RA. Gamma-aminobutyric acid: role in primary afferent depolarization. Science. 1972; 176:1043–1045. [PubMed: 4338197]
23. Doyle MW, Andresen MC. Reliability of monosynaptic sensory transmission in brain stem neurons in vitro. Journal of Neurophysiology. 2001; 85:2213–2223. [PubMed: 11353036]
24. Eccles JC, Schmidt R, Willis WD. Pharmacological studies on presynaptic inhibition. Journal of Physiology. 1963; 168:500–530. [PubMed: 14067941]
25. Jonas P, Bischofberger J, Sandkühler J. Corelease of two fast neurotransmitters at a central synapse. Science. 1998; 281:419–424. [PubMed: 9665886]
26. Kuno M. Mechanism of facilitation and depression of the excitatory synaptic potential in spinal motoneurones. Journal of Physiology. 1964; 175:100–112. [PubMed: 14241151]
27. Clements JD, Forsythe ID, Redman SJ. Presynaptic inhibition of synaptic potentials evoked in cat spinal motoneurones by impulses in single group Ia axons. Journal of Physiology. 1987; 383:153–169. [PubMed: 2821234]
28. Li Y, Burke RE. Short-term synaptic depression in the neonatal mouse spinal cord: effects of calcium and temperature. Journal of Neurophysiology. 2001; 85:2047–2062. [PubMed: 11353021]
29. Abbott LF, Varela JA, Sen K, Nelson SB. Synaptic depression and cortical gain control. Science. 1997; 275:221–224.
30. Seki K, Perlmutter SI, Fetz EE. Sensory input to primate spinal cord is presynaptically inhibited during voluntary movement. Nature Neuroscience. 2003; 6:1309–1316. [PubMed: 14625555]
31. Azim E, Jiang J, Alstermark B, Jessell TM. Skilled reaching relies on a V2a propriospinal internal copy circuit. Nature. 2014
32. Whishaw IQ. An endpoint, descriptive, and kinematic comparison of skilled reaching in mice (Mus musculus) with rats (Rattus norvegicus). Behavioural Brain Research. 1996; 78:101–111. [PubMed: 8864042]
33. Farr TD, Liu L, Colwell KL, Whishaw IQ, Metz GA. Bilateral alteration in stepping pattern after unilateral motor cortex injury: a new test strategy for analysis of skilled limb movements in neurological mouse models. Journal of Neuroscience Methods. 2006; 153:104–113. [PubMed: 16309746]
34. Prochazka A. Quantifying Proprioception. Progress in Brain Research. 1999; 123:133–142. [PubMed: 10635710]
35. Laughlin SB. Matching coding, circuits, cells, and molecules to signals: general principles of retinal design in the fly's eye. Progress in Retinal and Eye Research. 1994; 13:165–196.

36. Brenner N, Bialek W, de Ruyter van Steveninck R. Adaptive rescaling maximizes information transmission. Neuron. 2000; 26:695–702. [PubMed: 10896164]
37. Eccles JC, Kostyuk PG, Schmidt RF. Central pathways responsible for depolarization of primary afferent fibres. Journal of Physiology. 1962; 161:237–257. [PubMed: 13889054]
38. Tian N, et al. The role of the synthetic enzyme GAD65 in the control of neuronal gamma-aminobutyric acid release. Proceedings of the National Academy of Sciences. 1999; 96:12911–12916.
39. Churchland MM, Lisberger SG. Experimental and computational analysis of monkey smooth pursuit eye movements. Journal of Neurophysiology. 2001; 86:741–759. [PubMed: 11495947]
40. Baker SN. Oscillatory interactions between sensorimotor cortex and the periphery. Current Opinion in Neurobiology. 2007; 17:649–655. [PubMed: 18339546]
41. Llinás RR. Inferior olive oscillation as the temporal basis for motricity and oscillatory reset as the basis for motor error correction. Neuroscience. 2009; 162:797–804. [PubMed: 19393291]
42. Whitmer D, et al. High frequency deep brain stimulation attenuates subthalamic and cortical rhythms in Parkinson's disease. Front. Hum. Neurosci. 2012; 6
43. Evans CM, Fellows SJ, Rack PM, Ross HF, Walters DK. Response of the normal human ankle joint to imposed sinusoidal movements. Journal of Physiology. 1983; 344:483–502. [PubMed: 6655591]
44. Gosgnach S, et al. V1 spinal neurons regulate the speed of vertebrate locomotor outputs. Nature. 2006; 440:215–219. [PubMed: 16525473]
45. Akay T, Fouad K, Pearson KG. New technique for drug application to the spinal cord of walking mice. J. Neurosci. Methods. 2008; 171:39–47. [PubMed: 18355923]
46. Bui TV, et al. Circuits for grasping: spinal dI3 interneurons mediate cutaneous control of motor behavior. Neuron. 2013; 78:191–204. [PubMed: 23583114]
47. Rudomin P, Jimenez I, Solodkin M, Duenas S. Sites of action of segmental and descending control of transmission on pathways mediating PAD of Ia- and Ib-afferent fibers in cat spinal cord. Journal of Neurophysiology. 1983; 50:743–769. [PubMed: 6313870]
48. Lomelí J, Quevedo J, Linares P, Rudomin P. Local control of information flow in segmental and ascending collaterals of single afferents. Nature. 1998; 395:600–604. [PubMed: 9783585]
49. Hultborn H, Meunier S, Pierrot-Deseilligny E, Shindo M. Changes in presynaptic inhibition of Ia fibres at the onset of voluntary contraction in man. Journal of Physiology. 1987; 389:757–772. [PubMed: 3681742]
50. Nielsen J, Kagamihara Y. The regulation of presynaptic inhibition during co-contraction of antagonistic muscles in man. Journal of Physiology. 1993; 464:575–593. [PubMed: 8229819]

Supplementary References

51. Wichterle H, Lieberam I, Porter JA, Jessell TM. Directed differentiation of embryonic stem cells into motor neurons. Cell. 2002; 110:385–397. [PubMed: 12176325]
52. Shneider NA, Mentis GZ, Schustak J, O'Donovan MJ. Functionally reduced sensorimotor connections form with normal specificity despite abnormal muscle spindle development: the role of spindle-derived neurotrophin 3. Journal of Neuroscience. 2009; 29:4719–4735. [PubMed: 19369542]
53. Hantman AW, Jessell TM. Clarke's column neurons as the focus of a corticospinal corollary circuit. Nature Neuroscience. 2010; 13:1233–1239. [PubMed: 20835249]
54. Varela JA, et al. A quantitative description of short-term plasticity at excitatory synapses in layer 2/3 of rat primary visual cortex. Journal of Neuroscience. 1997; 17:7926–7940. [PubMed: 9315911]
55. Clements JD, Silver RA. Unveiling synaptic plasticity: a new graphical and analytical approach. Trends in Neurosciences. 2000; 23:105–113. [PubMed: 10675910]
56. Burke RE, Rudomin P. Spinal Neurons and Synapses. The Handbook of Physiology. The Nervous System. 1977; 1:877–944.

57. Bawa P, Stein RB. Frequency response of human soleus muscle. Journal of Neurophysiology. 1976; 39:788–793. [PubMed: 966038]

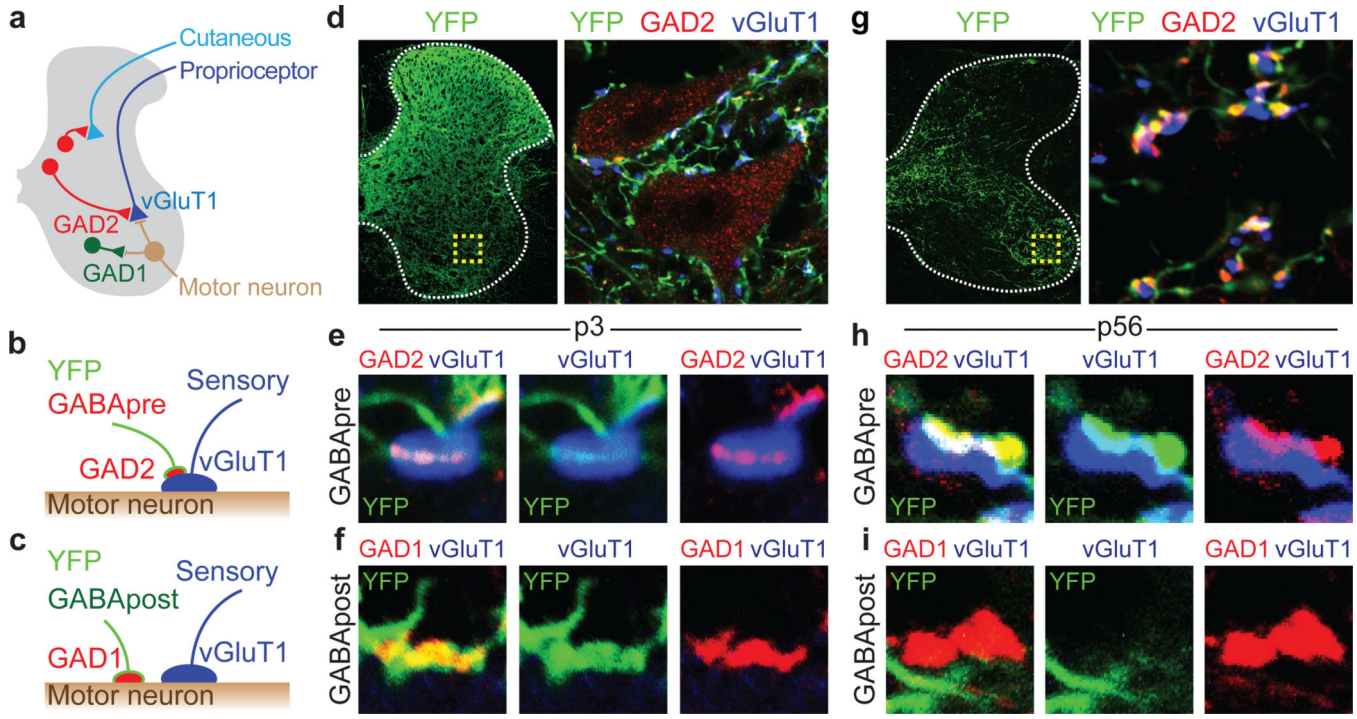

Figure 1. Genetic targeting of GABApre neurons

a, GABApre contacts on sensory terminals; GABApost contacts on motor neurons. **b,** GABApre: GAD2^{+}/GAD1^{+} boutons on vGluT1^{+} proprioceptor terminals. **c,** GABApost: GAD2^{OFF}/GAD1^{+} boutons not on vGluT1^{+} terminals. **d–f,** p3 *FLEX-ChR2-YFP* lumbar injection in *Gad2*^{Cre} mice. **d,** Ventral horn (box): YFP^{+}/GAD2^{+} GABApre boutons contact vGluT1^{+} proprioceptor terminals (**e,** high resolution); YFP^{+}/GAD1^{+} GABApost boutons do not contact vGluT1^{+} terminals (**f**). p0–3 injection marks GABApre (85.2 ± 2.1%) and GABApost (57.3 ± 3.4%; *n* = 3) boutons. **g–i,** p56 *FLEX-ChR2-YFP* cervical injection in *Gad2*^{Cre} mice. **g,** Ventral horn (box): YFP^{+}/GAD2^{+} GABApre boutons contact vGluT1^{+} terminals (**h**); **i,** YFP^{OFF}/GAD1^{+} GABApost bouton. p56–84 injection marks GABApre (77.6 ± 8.5%) but not GABApost boutons (1.0 ± 0.1%; *n* = 2). Values and error bars, mean ± s.e.m.

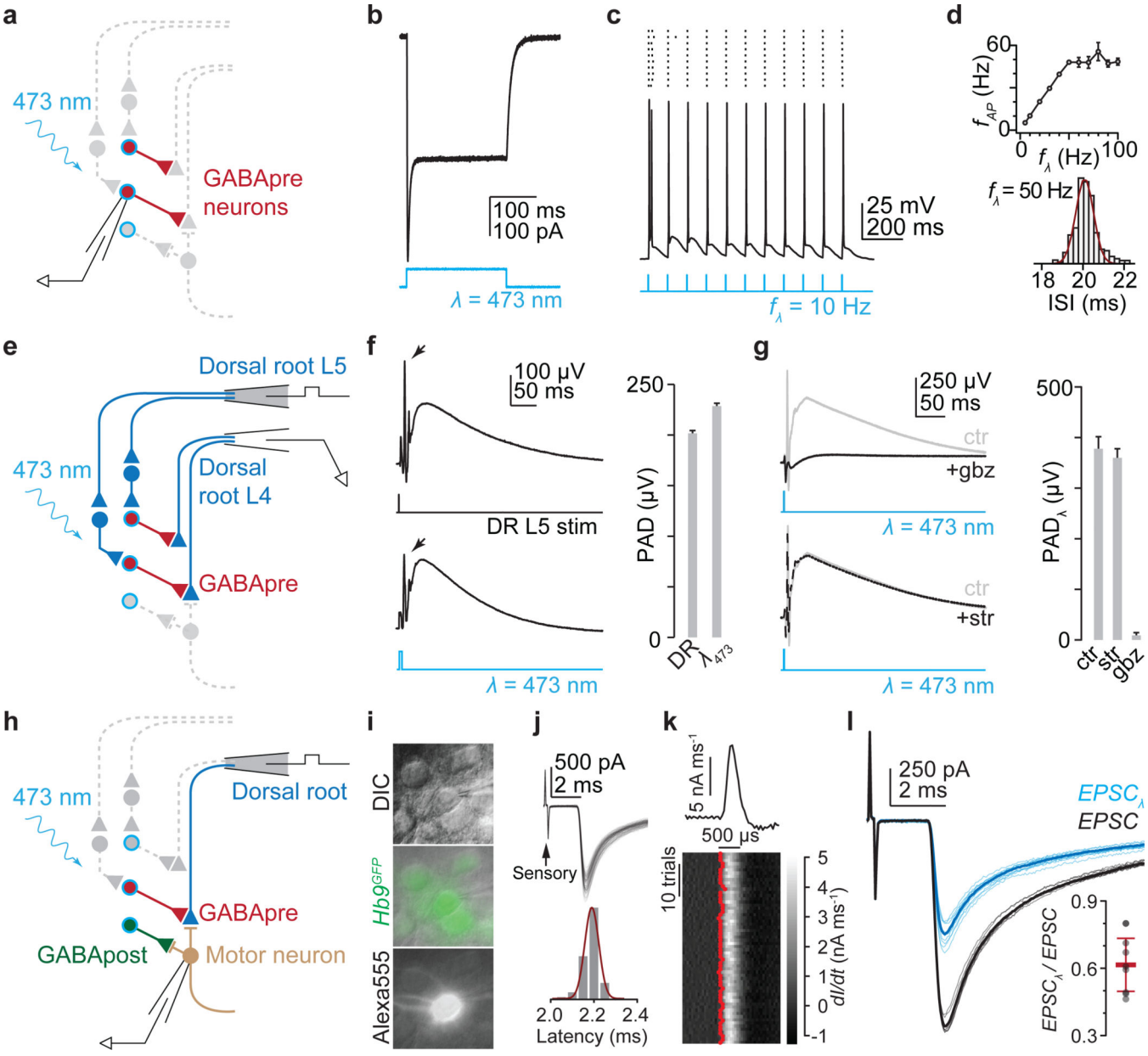

Figure 2. *Gad2*^{Cre} photoactivation elicits presynaptic inhibition

a, Recording from ChR2-YFP^{+} (blue outline) *Gad2*^{Cre} neurons (red). **b,** Photostimulation (λ) induced currents and **c,** action potentials, **d,** whose frequency (f_{AP}) followed light-pulse frequency (f_{λ}) up to ~50 Hz (n = 3). **e,** Dorsal root stimulation (L5) and recording (L4). **f,** L5-evoked (top, DR) and light-evoked (bottom, λ_{473}; n = 4) PAD. Arrows, antidromic spikes. **g,** Light-evoked PAD without (ctr) and with SR 95531 (gbz, 2 µM) or strychnine (str, 5 µM). Plots (**f**, **g**) show PAD amplitude. **h,** Isolating sensory input during *Gad2*^{Cre} photoactivation. **i,** Motor neuron identified using DIC optics, *Hb9*^{GFP} expression and Alexa^{555} fill. **j,** Monosynaptic sensory-EPSCs (90 trials, 10 Hz); onset latencies (Gaussian fit, red) estimated using, **k,** EPSC waveform derivative (top, mean; bottom, individual traces; EPSC onsets, red). Mean onset latency 2.87 ± 0.18 ms; cv_{onset} 0.018 ± 0.002; n = 19.

l, Sensory-EPSCs (0.1 Hz; mean, bold; raw, faint) without (*EPSC*, black) or with photoactivation ($EPSC_{\lambda}$, blue; fifteen 1 ms pulses; 50 Hz; 45 ms delay). Inset, EPSC suppression; $n = 9$. Values and error bars, mean ± s.e.m., except **l,** mean ± s.d. See Extended Data Figs 2,4 for additional quantification.

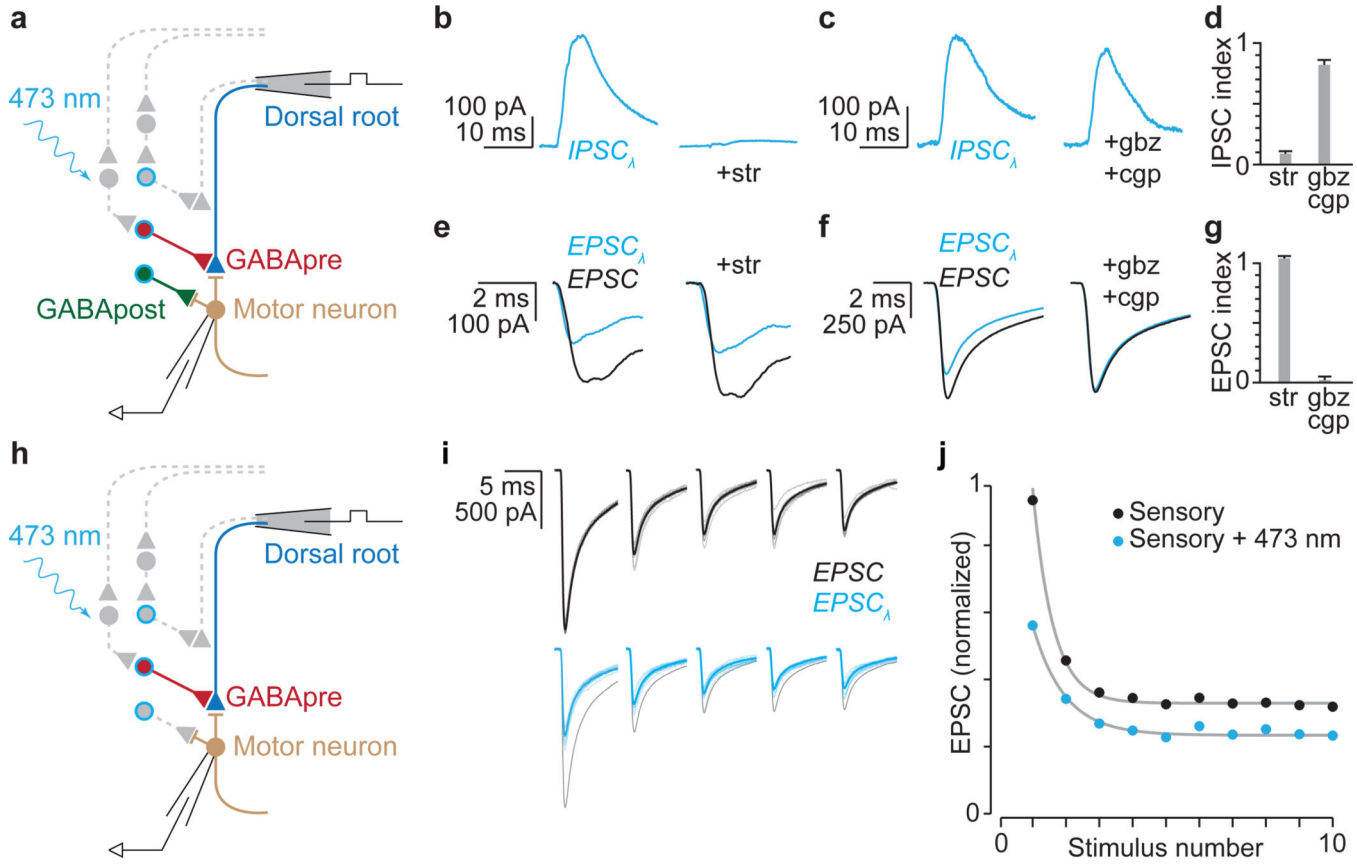

Figure 3. GABApre photoactivation reduces sensory transmitter release

a, Distinguishing GABApre from GABApost inhibition. **b–g,** Pharmacological analysis: **b–d,** light-evoked (λ) IPSCs, **b,** strychnine (str; *n* = 5), **c,** SR 95531 (gbz; *n* = 3) and CGP 54626 (cgp, 2.5 μM; *n* = 3), **d,** IPSC index: ratio of IPSC amplitude with drug to control; **e–g,** *Gad2*^{Cre} suppression of sensory-EPSCs (with photostimulation, blue; without, black), **e,** (str, *n* = 3), **f,** (gbz/cgp, *n* = 4), **g,** EPSC index: no effect = 1; drug abolishes EPSC-suppression = 0 (see Methods for description and Extended Data Fig. 5 for statistics). **h,** Isolation of GABApre inhibitory action. **i,** Sensory-EPSCs (10 pulses, 25 Hz; mean, bold; raw, faint) without (black) or with photostimulation (blue, black control superimposed for comparison). **j,** Normalized mean EPSC amplitudes from **i**. Grey, exponential fits to model-generated EPSC amplitudes. Values and error bars, mean ± s.e.m.

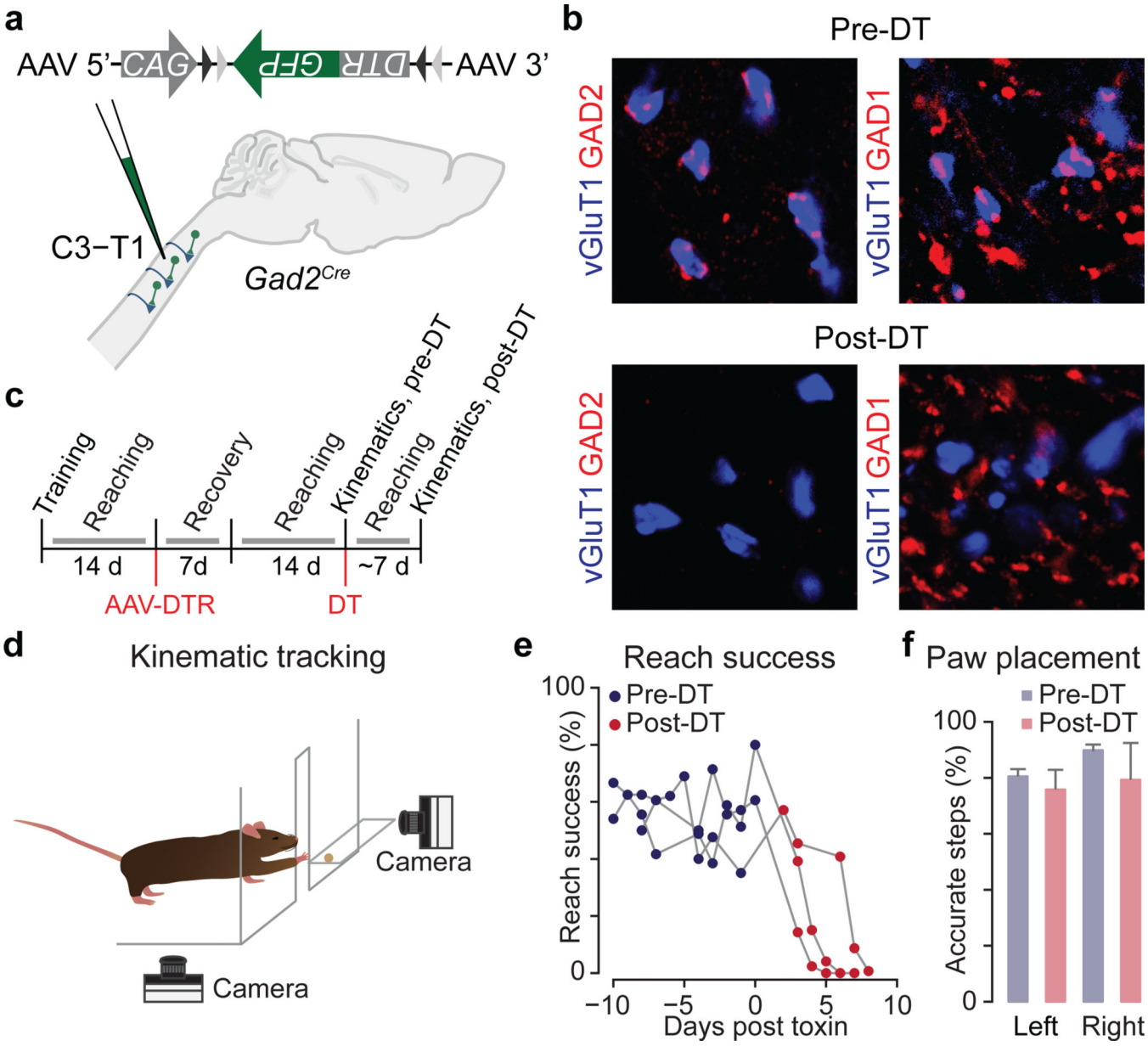

Figure 4. Selective GABApre ablation

a, After C3–T1 *FLEX-DTR-GFP* injection into adult *Gad2*^{Cre} mice, **b,** GABApre boutons (GAD2^{+}, red) contact proprioceptor terminals (vGluT1^{+}, blue) pre- but not post-DT. Only GAD1-marked GABApost boutons remain post-DT. vGluT1^{+} boutons with GABApre contacts, pre-DT 88 ± 2% (*n* = 2,058 boutons in 4 mice); post-DT 9 ± 1% (*n* = 4,347 boutons in 3 mice). **c,** Experimental timeline. **d,** Reaching kinematics assay (see Methods)[31]. **e,** Reach success pre-DT and post-DT (3 mice shown). **f,** Stepping accuracy, horizontal ladder assay[33]. Values and error bars, mean ± s.e.m. See Extended Data Fig. 9 and Extended Data Table 1 for statistics.

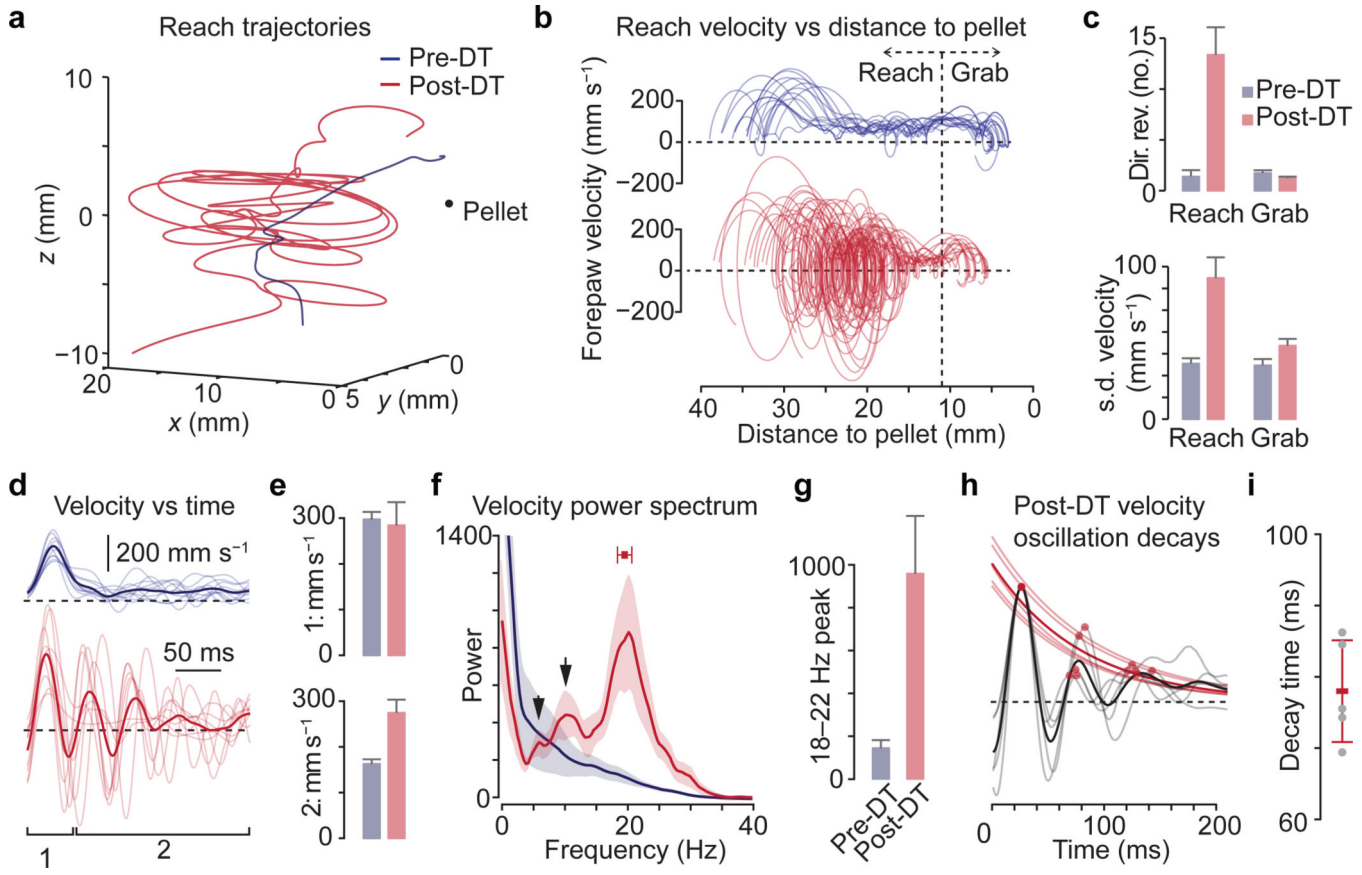

Figure 5. GABApre ablation uncovers limb oscillation during reaching

a, Reach trajectories and **b,** velocities from a representative mouse. Vertical line, reach versus grab phases. Horizontal line, forepaw direction reversals (also in **d,h**). **c,** Direction reversals and s.d. of velocity between reaches during reach and grab phases (*n* = 4 mice, 112 reaches). **d,** Paw velocity versus time from a second representative mouse. Mean, bold; individual reaches, faint. **e,** Peak reach velocities: initial (bracket '1' in **d**) and subsequent (>50 ms, bracket '2' in **d**). **f,** Mean power spectra of reach velocities; shaded area, s.e.m. Red box, mean frequency peak ± s.d. Arrows, subharmonic peaks. **g,** Peak power: 18–22 Hz (*n* = 5 mice, 132 reaches; see Methods). **h,** Peak-aligned averages within (grey) and across mice (black). Mean velocity peaks for each mouse (red dots) and exponential fits (faint red lines). Mean fit, bold red line,. **i,** Decay time constant across mice (mean ± s.d.; *n* = 5).Values and error bars, mean ± s.e.m., except where indicated. See Extended Data Table 1 for statistics.

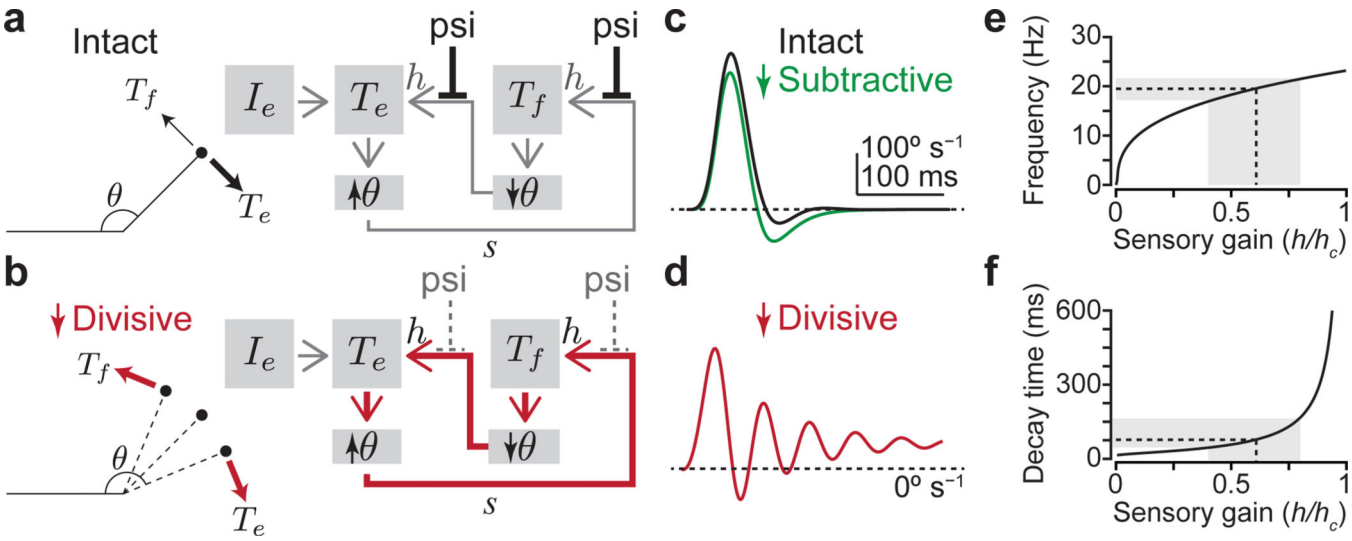

Figure 6. GABApre neurons regulate sensory gain

a,b, Model of joint angle, θ, under the control of flexor T_f and extensor T_e torques. External drive I_e activates T_e, increasing θ (bold arrow). Sensory feedback *s* recruits a counteracting T_f with efficacy specified by sensory gain *h*. Presynaptic inhibition (psi) suppresses gain divisively, keeping T_f small (faint arrow, **a**). With reduced psi, high gain feedback induces alternating, sensory-driven T_f and T_e (red arrows, **b**). **c,d,** Joint angle velocity over time for, **c**, intact (h/h_c = 0.1) and reduced subtractive (postsynaptic) inhibition (green line, see Methods), and **d**, high gain (h/h_c = 0.6, reduced divisive psi). For gains above the critical level (h_c), oscillations do not decay. **e,** Oscillation frequency and, **f**, decay time versus gain. Grey boxes, range of gain values (h/h_c = 0.4–0.8) corresponding to post-DT oscillation frequencies and decay times (Fig. 5d–i). Dashed lines, 19.5 Hz, 77 ms. See Supplementary Note 4.